Journal of Computational Physics 415 (2020) 109515

Contents lists available at ScienceDirect

Journal of Computational Physics

www.elsevier.com/locate/jcp

Techniques for improving monotonicity in a fourth-order finite-volume algorithm solving shocks and detonations

L.D. Owen *, X. Gao, S.M. Guzik

CFD & Propulsion Laboratory, Colorado State University, Fort Collins, CO 80523, USA

ARTICLE INFO

Article history:
Received 7 May 2019
Received in revised form 13 April 2020
Accepted 26 April 2020
Available online 5 May 2020

Keywords:
High-order finite-volume method
Nonlinear PDEs
Compressible multispecies flows
Non-oscillating techniques
Shock and detonation waves
Adaptive mesh refinement

ABSTRACT

Techniques are proposed to reduce numerical oscillations in a fourth-order, finite-volume algorithm for solving thermally-perfect, reacting fluid flows with strong discontinuities, such as shock or detonation waves. These additional mechanisms have proven necessary for multispecies flows solved at fourth-order accuracy, and contribute towards bounding the variation of the solution in the vicinity of strong discontinuities. There, oscillations can form due to strong gradients in the flow and may be further intensified by numerical procedures introduced to treat the thermally-perfect thermodynamic system and physical constraints on species mass fractions. The new techniques are designed to respect the conservative property of the base algorithm, retain fourth-order accuracy of the solution in regions of smooth flow, and cooperate with the high-order piecewise parabolic method limiter. Extensive numerical tests, ranging from multispecies mixing flows to reacting flows with detonations, are performed to verify that the new techniques meet the design criteria while effectively suppressing oscillations. The proposed techniques are applied to solve the Shu-Osher and double Mach reflection problems and a set of oblique detonation wave problems. The results demonstrate the effectiveness and robustness of the algorithm.

1. Introduction

Finite-volume methods (FVMs) are inherently conservative and benefit from computational efficiency on structured grids. Traditionally, FVMs in computational fluid dynamics (CFD) engineering applications have been constrained to second-order accuracy because high-order methods are more complicated and lack the significant research investment of second-order methods [1,2]. However, increasing the order of accuracy of an algorithm from second-order to higher order (e.g., fourth-order, which is of interest to the present study) has the potential to deliver higher accuracy on a given mesh. This is particularly important when solving flows that contain unsteady vortices, complex dynamics, or small scale resolvable features, such as those encountered in large-eddy simulation, where low-order algorithms are overly diffusive. Additionally, high-order methods can take advantage of modern computational hardware in terms of increasing the arithmetic intensity for the same level of accuracy.

In recent years, interest in the development and application of high-order CFD methods has increased. International workshops on high-order methods offer an open forum for CFD researchers from academia, government, and industry to share the development and evaluation of high-order methods [3]. Nevertheless, extending FVMs from first or second-order

* Corresponding author.
E-mail address: Landon.Owen@colostate.edu (L.D. Owen).

https://doi.org/10.1016/j.jcp.2020.109515
0021-9991/

Nomenclature

c_n	Mass fraction of the nth species	$\boldsymbol{u}$	Velocity vector
$\boldsymbol{e}^d$	Unit normal vector in the dth direction	$\mathbf{W}$	Native primitive variable vector
$\vec{\mathbf{F}}$	Convective flux dyad, i.e., $[\mathbf{F}_x, \mathbf{F}_y, \mathbf{F}_z]$	$\widetilde{\mathbf{W}}$	Nonnative primitive variable vector
$\boldsymbol{i}$	Vector denoting a spatial index	x_d	Position in physical space in the dth direction
M_n	Molecular weight of the nth species	ρ	Density
N_r	Total number of reactions	ξ_d	Position in computational space in the dth direction
N_s	Total number of species		
p	Pressure	$\dot{\omega}_n$	Chemical production rate of the nth species
R_n	Gas constant for the nth species	$\langle\cdot\rangle_{\boldsymbol{i}}$	Cell-averaged value
T	Temperature	$\langle\cdot\rangle_{\boldsymbol{i}+\frac{1}{2}\boldsymbol{e}^d}$	Face-averaged value
$\mathbf{U}$	Conservative variable vector	$\cdot\vert_{(2)}$	Second-order value

to high-order accuracy increases the complexity of the algorithm and the potential for numerical oscillations in nonsmooth regions of fluid flow. Furthermore, these issues can be exacerbated when solving thermally-perfect, reacting, gaseous flows with shock and detonation waves. Many techniques have been developed to obtain solutions for flows containing shock or detonation waves in the context of high-order FVMs, including the piece-wise parabolic method (PPM) [4,5], essentially non-oscillatory (ENO) and weighted ENO (WENO) schemes [6,7], multi-dimensional limiting process [8,9], and hybrid limiters [10], to name a few. Many strategies often pose constraints in terms of the solution accuracy, computational efficiency, and algorithmic complexity. Compromises are sometimes made to increase monotonicity of an algorithm. One such compromise is when conservation is sacrificed in favor of a less oscillatory, quasi-conservative method (the double-flux method [11–13]). Another compromise, made in nonsmooth flow regions, is when a fifth-order, linear WENO scheme is replaced with a total variation diminishing limiter, such as the hybrid method [10], which blends a double-flux method [14], a superbee-centering approach [15], a nonlinear error controlled WENO method [16], a low Mach number adjustment [17], and a monotonic upwind scheme for conservation laws [18]. Published literature [19,20] also indicates that simply adding numerical dissipation is not sufficient to eliminate or mitigate problems that arise from strong nonlinearities of the thermodynamic system, and inconsistently added dissipation can potentially lead to decreased stability. In the present work, we develop techniques in "Chord" [21–24] using the PPM limiter as a basis to suppress numerical oscillations in discontinuous flows. There, an emphasis is made on using adaptive-mesh refinement (AMR) with fourth-order accuracy in space and time.

The primary goal of this paper is to develop and apply techniques to reduce numerical oscillations in high Reynolds number, multispecies flows with strong shock and detonation waves using a fourth-order FVM. The remainder of the paper is organized as follows. The mathematical and numerical modeling framework are briefly described in Section 2. The relevant numerical operations in the fourth-order FVM are detailed in Section 3. The new oscillation reduction techniques are provided in Section 4. Technical details of these new techniques are provided in Sections 4.2 and 4.3, including a description of the methodology and demonstrations of oscillation reduction through test cases. Section 5 provides verification and numerical solutions to the Shu-Osher problem [25], double Mach reflection problem, and a series of oblique detonation waves (ODWs) over a wedge to demonstrate the satisfactory performance of the techniques. Finally, Section 6 states the conclusions.

2. Mathematical and numerical modeling framework

2.1. Mathematical modeling

In this work, gaseous fluid flow is modeled using the Euler equations and a set of species transport equations with reaction kinetics, when combustion is considered. The computational domain is Cartesian, and the physical space is mapped to computational space using the generalized curvilinear coordinate transformation. Further, the grid is assumed to not deform over time. When transformed using grid metrics, the system of governing equations for a compressible gas on a mapped domain, including the continuity, momentum, energy, and a set of species transport equations, is given by

$$\frac{\partial}{\partial t}\left(J\rho\right) + \vec{\nabla}_\xi \cdot \left(\mathrm{N}^{\mathrm{T}}\rho\boldsymbol{u}\right) = 0\,, \tag{1}$$

$$\frac{\partial}{\partial t}\left(J\rho\boldsymbol{u}\right) + \vec{\nabla}_\xi \cdot \left(\mathrm{N}^{\mathrm{T}}(\rho\boldsymbol{u}\boldsymbol{u} + p\vec{\vec{I}})\right) = J\rho\vec{f}\,, \tag{2}$$

$$\frac{\partial}{\partial t}\left(J\rho e\right) + \vec{\nabla}_\xi \cdot \left(\mathrm{N}^{\mathrm{T}}\rho\boldsymbol{u}(e + \frac{p}{\rho})\right) = J\rho\vec{f}\cdot\boldsymbol{u}\,, \tag{3}$$

$$\frac{\partial}{\partial t}\left(J\rho c_n\right) + \vec{\nabla}_\xi \cdot \left(\mathrm{N}^{\mathrm{T}}\rho c_n\boldsymbol{u}\right) = J\rho\dot{\omega}_n\,, \quad n = 1, \ldots, N_s\,, \tag{4}$$

where J is the metric Jacobian, N^{T} is the transformation grid metrics, e is the total specific energy, $\vec{\vec{I}}$ is the identity tensor, and $\vec{f}$ is the body force terms. The total specific energy is given by

$$e = \frac{|\vec{u}|^2}{2} + \sum_{n=1}^{N_s} c_n h_n - \frac{p}{\rho}\,, \tag{5}$$

where h_n is the total specific enthalpy of the nth species. Additionally, the ideal gas law is

$$p = \rho T \sum_{n=1}^{N_s} R_n c_n\,. \tag{6}$$

The governing equations on mapped domains can be written in the conservative form as

$$\frac{\partial J\mathbf{U}}{\partial t} + \vec{\nabla}_\xi \cdot \left(\mathrm{N}^{\mathrm{T}}\vec{\mathbf{F}}\right) = J\mathbf{S}, \tag{7}$$

where $\mathbf{U}$ is the solution variable vector, $\vec{\mathbf{F}}$ is the convective flux dyad, and $\mathbf{S}$ is the source term vector; these are given by

$$\mathbf{U} = \begin{bmatrix} \rho \\ \rho\boldsymbol{u} \\ \rho e \\ \rho c_n \end{bmatrix}, \vec{\mathbf{F}} = \begin{bmatrix} \rho\boldsymbol{u} \\ \rho\boldsymbol{u}\boldsymbol{u} + p\vec{\vec{I}} \\ \rho\boldsymbol{u}\,(e + p/\rho) \\ \rho c_n \boldsymbol{u} \end{bmatrix}, \mathbf{S} = \begin{bmatrix} 0 \\ \rho\vec{f} \\ \rho\vec{f}\cdot\boldsymbol{u} \\ \rho\dot{\omega}_n \end{bmatrix}. \tag{8}$$

Additionally, we define the primitive variables as $\mathbf{W} = [\rho\,, \boldsymbol{u}\,, p\,, c_n]^{\mathrm{T}}$, and the nonnative primitive variables are $[\widetilde{\mathbf{W}}]^{\mathrm{T}} = [\mathbf{W}^{\mathrm{T}}, T]^{\mathrm{T}}$.

The thermodynamic must be approximated to close the system of governing equations. Under the thermally-perfect fluid assumption, the thermodynamic properties (such as enthalpy and specific heat) are functions of temperature. For each species, the properties are evaluated using curve fit polynomials [26,27]. For example, the enthalpy of the nth species is computed using

$$h_n(T) = R_n T \left(\frac{a_{8,n}}{T} - \frac{a_{1,n}}{T^2} + \frac{a_{2,n}}{T}\ln T + \sum_{i=3}^{7} \frac{a_{i,n}}{i-2} T^{(i-3)} \right), \tag{9}$$

where the coefficients $a_{1,n}$ to $a_{8,n}$ are empirically fit over a set range of temperature. Typically, one set of coefficients is provided for a range of $200 - 1000$ K and another for a range of $1000 - 6000$ K. This means that Eq. (9) is only valid for $200\ \mathrm{K} < T < 6000$ K. The properties of the gaseous mixture are evaluated using certain mixing rules. For example, the total specific enthalpy for the fluid mixture is $h = \sum_{n=1}^{N_s} c_n h_n$.

2.2. Numerical framework

To solve the nonlinear system of governing partial differential equations of Eq. (7), a semi-discrete form is derived for each cell i using the finite-volume method as

$$\frac{\mathrm{d}}{\mathrm{d}t}\langle J\mathbf{U}\rangle_{\boldsymbol{i}} = -\frac{1}{h}\sum_{d=1}^{D}\left(\langle \mathrm{N}_d^{\mathrm{T}}\vec{\mathbf{F}}\rangle_{\boldsymbol{i}+\frac{1}{2}\boldsymbol{e}^d} - \langle \mathrm{N}_d^{\mathrm{T}}\vec{\mathbf{F}}\rangle_{\boldsymbol{i}-\frac{1}{2}\boldsymbol{e}^d}\right) + \langle J\mathbf{S}\rangle_{\boldsymbol{i}}\,, \tag{10}$$

where $\langle \mathrm{N}_d^{\mathrm{T}}\vec{\mathbf{F}}\rangle_{\boldsymbol{i}+\frac{1}{2}\boldsymbol{e}^d}$ is the mapped convective fluxes and $\langle J\mathbf{S}\rangle_{\boldsymbol{i}}$ is the mapped source term. Again, we employ FVMs because we are interested in solving flows with strong discontinuities on locally-structured grids with AMR [28]. These flows benefit from the conservation property of FVMs. Other spatial discretization methods, such as finite-difference, finite-element, discontinuous Galerkin, or lattice-Boltzmann, can also be used for solving the system of equations. Readers are referred to literature [29–32] for strengths and limitations of each method. The time evolution of the solution is achieved using the standard, four-stage Runge-Kutta (RK4) time marching method [33]. While monotonic fluxes at each stage of the standard RK4 methods does not guarantee stability of the updated solution, the present work focuses on reducing numerical oscillations associated with the fourth-order spatial discretization scheme. More stable time-marching methods, such as the flux-corrected transport method [34], will be considered in future work.

Although this research contains no new work on AMR, all functionality in the present work is implemented in an AMR framework to allow solutions to utilize AMR. Parallel AMR in Chord makes use of the Chombo library [5,28]. AMR allows increased mesh resolution at areas of interest without the increased computational costs associated with having increased mesh resolution throughout the entire domain. Areas of interest, such as combustion flame fronts, should use a finer mesh to reduce the error. Time marching on refined levels can employ sub-cycling, meaning the solution on the finer level advances multiple smaller time steps relative to the coarser level solution. Additionally, all solutions in this work

utilize artificial viscosity in the vicinity of shocks. More information about the sub-cycling and artificial viscosity techniques used are provided by Guzik et al. [21]. Details regarding the numerical framework of Chord can be found in previous work [21–24].

3. Numerical operators

This section details the numerical operations relevant to the techniques that will be presented in Section 4. The numerical oscillations of interest to this work fundamentally reside with the spatial operators in the present fourth-order FVM algorithm when solving flows with strong discontinuities. First, we discuss the fourth-order deconvolution/convolution (DC) operators, since they are extensively used in the present algorithm and are prone to introduce numerical oscillations, as demonstrated in Section 4.3. Next, we outline the methodology for computing the fourth-order, mapped, convective fluxes. Finally, we present the nonlinear physics and the techniques for constraining species mass concentrations and mass fractions.

3.1. Deconvolution/convolution operators

Most second-order FVMs use the midpoint rule to approximate cell-averaged or face-averaged data, meaning $\langle\phi\rangle_{\boldsymbol{i}} = \phi_{\boldsymbol{i}} + \mathcal{O}(\Delta\xi^2)$, where ϕ can be any quantity, $\langle\phi\rangle_{\boldsymbol{i}}$ is a cell-averaged value, $\phi_{\boldsymbol{i}}$ is a cell-centered value, and $\Delta\xi$ is the spatial resolution in computational space. However, the fourth-order FVM in the present study uses a convolution operation to approximate the averaged value in a cell or at a face. The fourth-order convolution of a cell-centered value is used to approximate a cell-averaged value and is defined as

$$\langle\phi\rangle_{\boldsymbol{i}} = \phi_{\boldsymbol{i}} + \frac{\Delta\xi^2}{24}\Delta_{\xi}^{(2)}\phi_{\boldsymbol{i}} + \mathcal{O}\left(\Delta\xi^4\right), \tag{11}$$

where

$$\Delta_{\xi}^{(2)}\phi_{\boldsymbol{i}} = \sum_{d=1}^{D}\left(\frac{\partial^2\phi}{\partial\xi_d^2}\right)_{\boldsymbol{i}} = \sum_{d=1}^{D}\frac{\phi_{\boldsymbol{i}+\boldsymbol{e}^d} - 2\phi_{\boldsymbol{i}} + \phi_{\boldsymbol{i}-\boldsymbol{e}^d}}{\Delta\xi_d^2}. \tag{12}$$

Correspondingly, the fourth-order deconvolution of a cell-averaged value can be used to approximate a cell-centered value when conversion between averaged and point values is necessary and is defined as

$$\phi_{\boldsymbol{i}} = \langle\phi\rangle_{\boldsymbol{i}} - \frac{\Delta\xi^2}{24}\Delta_{\xi}^{(2)}\langle\phi\rangle_{\boldsymbol{i}} + \mathcal{O}\left(\Delta\xi^4\right). \tag{13}$$

Equations (11) and (13) are referred to as the convolution and deconvolution operators in cells, respectively. The convolution of a face-centered value is used to approximate a face-averaged value and is defined as

$$\langle\phi\rangle_{\boldsymbol{i}+\frac{1}{2}\boldsymbol{e}^d} = \phi_{\boldsymbol{i}+\frac{1}{2}\boldsymbol{e}^d} + \frac{\Delta\xi^2}{24}\Delta_{\xi}^{(\perp,d)}\phi_{\boldsymbol{i}+\frac{1}{2}\boldsymbol{e}^d} + \mathcal{O}\left(\Delta\xi^4\right), \tag{14}$$

where $\langle\phi\rangle_{\boldsymbol{i}+\frac{1}{2}\boldsymbol{e}^d}$ is a face-averaged value, $\phi_{\boldsymbol{i}+\frac{1}{2}\boldsymbol{e}^d}$ is a face-centered value, and

$$\begin{aligned}\Delta_{\xi}^{(\perp,d)}\langle\phi\rangle_{\boldsymbol{i}+\frac{1}{2}\boldsymbol{e}^d} &= \sum_{d'\neq d}^{D}\left(\frac{\partial^2\langle\phi\rangle}{\partial\xi_{d'}^2}\right)_{\boldsymbol{i}+\frac{1}{2}\boldsymbol{e}^d} \\ &= \sum_{d'\neq d}^{D}\frac{\langle\phi\rangle_{\boldsymbol{i}+\frac{1}{2}\boldsymbol{e}^d+\boldsymbol{e}^{d'}} - 2\langle\phi\rangle_{\boldsymbol{i}+\frac{1}{2}\boldsymbol{e}^d} + \langle\phi\rangle_{\boldsymbol{i}+\frac{1}{2}\boldsymbol{e}^d-\boldsymbol{e}^{d'}}}{\Delta\xi_{d'}^2}.\end{aligned} \tag{15}$$

Similarly, the deconvolution of a face-averaged value can be used to approximate a face-centered value when conversion between averaged and point values is necessary and is defined as

$$\phi_{\boldsymbol{i}+\frac{1}{2}\boldsymbol{e}^d} = \langle\phi\rangle_{\boldsymbol{i}+\frac{1}{2}\boldsymbol{e}^d} - \frac{\Delta\xi^2}{24}\Delta_{\xi}^{(\perp,d)}\langle\phi\rangle_{\boldsymbol{i}+\frac{1}{2}\boldsymbol{e}^d} + \mathcal{O}\left(\Delta\xi^4\right). \tag{16}$$

The product of cell-averaged or face-averaged values also require convolution operations. The product of two cell-averaged values is evaluated by

$$\langle\phi\psi\rangle_{\boldsymbol{i}} = \langle\phi\rangle_{\boldsymbol{i}}\langle\psi\rangle_{\boldsymbol{i}} + \frac{\Delta\xi^2}{12}\sum_{d=1}^{D}\left(\frac{\partial\langle\phi\rangle}{\partial\xi_d}\right)_{\boldsymbol{i}}\left(\frac{\partial\langle\psi\rangle}{\partial\xi_d}\right)_{\boldsymbol{i}} + \mathcal{O}\left(\Delta\xi^4\right), \tag{17}$$

where ψ can be any quantity and

$$\left(\frac{\partial\langle\phi\rangle}{\partial\xi_d}\right)_{\boldsymbol{i}} = \frac{\langle\phi\rangle_{\boldsymbol{i}+\boldsymbol{e}^d} - \langle\phi\rangle_{\boldsymbol{i}-\boldsymbol{e}^d}}{2\Delta\xi_d}. \tag{18}$$

The product of two face-averaged values is

$$\langle\phi\psi\rangle_{\boldsymbol{i}+\frac{1}{2}\boldsymbol{e}^d} = \langle\phi\rangle_{\boldsymbol{i}+\frac{1}{2}\boldsymbol{e}^d}\langle\psi\rangle_{\boldsymbol{i}+\frac{1}{2}\boldsymbol{e}^d} + \frac{\Delta\xi^2}{12}\sum_{d'\neq d}^{D}\left(\frac{\partial\langle\phi\rangle}{\partial\xi_{d'}}\right)_{\boldsymbol{i}+\frac{1}{2}\boldsymbol{e}^d}\left(\frac{\partial\langle\psi\rangle}{\partial\xi_{d'}}\right)_{\boldsymbol{i}+\frac{1}{2}\boldsymbol{e}^d} + \mathcal{O}\left(\Delta\xi^4\right), \tag{19}$$

where

$$\left(\frac{\partial\langle\phi\rangle}{\partial\xi_{d'}}\right)_{\boldsymbol{i}+\frac{1}{2}\boldsymbol{e}^d} = \frac{\langle\phi\rangle_{\boldsymbol{i}+\frac{1}{2}\boldsymbol{e}^d+\boldsymbol{e}^{d'}} - \langle\phi\rangle_{\boldsymbol{i}+\frac{1}{2}\boldsymbol{e}^d-\boldsymbol{e}^{d'}}}{2\Delta\xi_{d'}}. \tag{20}$$

3.2. Solution procedure

The following 14 steps prescribe the solution procedure for evaluating the convective fluxes.

S.1 Calculate the second-order, nonnative primitive state (which includes temperature),

$$\left(\widetilde{\mathbf{W}}|_{(2)}\right)_{\boldsymbol{i}} = \mathbf{W}\left(\langle\mathbf{U}\rangle_{\boldsymbol{i}}\right). \tag{21}$$

S.2 Approximate the fourth-order accurate, cell-centered conservative state, $\mathbf{U}$, using

$$\mathbf{U}_{\boldsymbol{i}} = \langle\mathbf{U}\rangle_{\boldsymbol{i}} - \frac{\Delta\xi^2}{24}\Delta_{\xi}^{(2)}\langle\mathbf{U}\rangle_{\boldsymbol{i}}. \tag{22}$$

S.3 Directly calculate the cell-centered nonnative primitive state,

$$\widetilde{\mathbf{W}}_{\boldsymbol{i}} = \mathbf{W}\left(\mathbf{U}_{\boldsymbol{i}}\right). \tag{23}$$

S.4 Approximate the fourth-order accurate, cell-averaged nonnative primitive state using

$$\langle\widetilde{\mathbf{W}}\rangle_{\boldsymbol{i}} = \widetilde{\mathbf{W}}_{\boldsymbol{i}} + \frac{\Delta\xi^2}{24}\Delta_{\xi}^{(2)}\left(\widetilde{\mathbf{W}}|_{(2)}\right)_{\boldsymbol{i}}. \tag{24}$$

S.5 Interpolate the fourth-order accurate, face-averaged primitive state using Eq. (42)

S.6 Apply the slope flattening and PPM limiter [35,36] to the face-averaged primitive state. The PPM limiter modifies the interpolant on each cell adjacent face to constrain the parabolic profile in each cell. These techniques require the undivided, second-order second derivative, $\delta^2\mathbf{W}$. Note, these limiting methods are only necessary for certain types of flows, like flows with discontinuities.

S.7 Resolve the interpolated left and right states by solving a Riemann problem. Note that the solution to the Riemann problem depends on which variables of ρ, p, and T are interpolated and which is calculated using the ideal gas law (this is discussed further in Section 4.2). Numerical experimentation shows that limiting temperature and pressure and calculating density provides the largest reduction in numerical oscillations.

S.8 Calculate the second-order accurate temperature using the face-averaged native primitive state using

$$\left(T|_{(2)}\right)_{\boldsymbol{i}+\frac{1}{2}\boldsymbol{e}^d} = \frac{\langle p\rangle_{\boldsymbol{i}+\frac{1}{2}\boldsymbol{e}^d}}{\langle\rho\rangle_{\boldsymbol{i}+\frac{1}{2}\boldsymbol{e}^d}\sum_{n=1}^{N_s}R_n\langle c_n\rangle_{\boldsymbol{i}+\frac{1}{2}\boldsymbol{e}^d}}. \tag{25}$$

S.9 Deconvolve the face-centered primitive state from the face-averaged primitive state.

S.10 Calculate the face-centered temperature from the face-centered primitive state.

$$T_{\boldsymbol{i}+\frac{1}{2}\boldsymbol{e}^d} = \frac{p_{\boldsymbol{i}+\frac{1}{2}\boldsymbol{e}^d}}{\rho_{\boldsymbol{i}+\frac{1}{2}\boldsymbol{e}^d}\sum_{n=1}^{N_s}R_n\left(c_n\right)_{\boldsymbol{i}+\frac{1}{2}\boldsymbol{e}^d}}. \tag{26}$$

S.11 If the face-averaged temperature is required, as is the case for diffusive flows, convolve the face-averaged temperature using

$$\langle T\rangle_{\boldsymbol{i}+\frac{1}{2}\boldsymbol{e}^d} = T_{\boldsymbol{i}+\frac{1}{2}\boldsymbol{e}^d} + \frac{\Delta\xi^2}{24}\Delta_{\xi}^{(\perp,d)}\left(T|_{(2)}\right)_{\boldsymbol{i}+\frac{1}{2}\boldsymbol{e}^d}, \tag{27}$$

S.12 Calculate the face-centered convective flux dyad, $\vec{\mathbf{F}}$.
S.13 Convolve the face-centered convective flux dyad to find the face-averaged flux dyad, $\langle\vec{\mathbf{F}}\rangle$.
S.14 Solve the mapped, face-averaged convective fluxes using

$$\langle \mathrm{N}^{\mathrm{T}}\vec{\mathbf{F}}\rangle_{\boldsymbol{i}+\frac{1}{2}\boldsymbol{e}^d} = \langle \mathrm{N}^{\mathrm{T}}\rangle_{\boldsymbol{i}+\frac{1}{2}\boldsymbol{e}^d}\langle\vec{\mathbf{F}}\rangle_{\boldsymbol{i}+\frac{1}{2}\boldsymbol{e}^d} + \frac{\Delta\xi^2}{12}\sum_{d'\neq d}^{D}\left(\frac{\partial\langle \mathrm{N}^{\mathrm{T}}\rangle}{\partial\xi_{d'}}\right)_{\boldsymbol{i}+\frac{1}{2}\boldsymbol{e}^d}\left(\frac{\partial\vec{\mathbf{F}}}{\partial\xi_{d'}}\right)_{\boldsymbol{i}+\frac{1}{2}\boldsymbol{e}^d}. \tag{28}$$

3.3. Nonlinear physics

For calorically-perfect fluids, the primitive variable, T, can be explicitly computed from the conservative variables using

$$T = \frac{\gamma-1}{\sum_{n=1}^{N_s}\mathbf{U}_{(D+2+n)}R_n}\left(\mathbf{U}_{(D+2)} - \sum_{d=1}^{D}\frac{\mathbf{U}_{(d+1)}^2}{2\mathbf{U}_{(1)}}\right), \tag{29}$$

where $\mathbf{U}_{(i)}$ represents the ith component of the $\mathbf{U}$ vector from Eq. (8). However, for thermally-perfect, gaseous fluids, T is implicitly related to the internal energy from the function

$$f(\mathbf{U},T) = \sum_{d=1}^{D}\frac{\mathbf{U}_{(d+1)}^2}{2\mathbf{U}_{(1)}} + \sum_{n=1}^{N_s}\left(\mathbf{U}_{(D+2+n)}\big(h_n(T) - R_nT\big)\right) - \mathbf{U}_{(D+2)}. \tag{30}$$

Solving for T from Eq. (30) requires an iterative solution. In the present work, the Brent's method [37] is utilized to solve for temperature using $f(\mathbf{U},T)=0$. The solution in Brent's method is converged only if the following is true

$$\big|T_{\text{new}} - T_{\text{old}}\big| \leq \big(4\epsilon_1\big|T_{\text{new}}\big| + \epsilon_2\big), \tag{31}$$

where ϵ_1 and ϵ_2 are 3×10^{-15} and 1×10^{-12}, respectively.

The enthalpy term, $h_n(T)$, in Eq. (30) is computed using the curve fit polynomials from Eq. (9). As previously mentioned, these polynomials are only valid within a given range of temperature. Therefore, Brent's method will fail to converge to a value of T if it falls outside of the temperature range of the polynomial fits; in Section 4.3, we demonstrate how severe numerical oscillations can cause temperature to fall outside valid temperature range.

3.4. Physical constraints

The physical constraints on mass fractions are

$$\sum_{n=1}^{N_s}c_n = 1 \quad\text{and}\quad 0\leq c_n\leq 1, \quad \forall n\in N_s. \tag{32}$$

The first physical constraint in Eq. (32) is adhered to due to the law of mass conservation, but positivity of c_n is not inherently ensured due to numerical errors; therefore, the physical constraints must be explicitly enforced. There are many different ways to enforce Eq. (32). One common practice is to simply modify the mass fraction of a single inert species to meet the physical constraints. However, this technique can result in significant changes to enthalpy estimates and lead to divergence of Eq. (30). Instead, the physical constraints are enforced by correcting all present species depending on the relative quantity of each species, so the more mass concentration or mass fraction of a particular species that exists in a cell or at a face, the more that species is adjusted. The correction of species mass concentrations is done using

$$(\rho c_n)^f = \frac{(\widetilde{\rho c_n})\,\rho}{\sum_{j=1}^{N_s}\widetilde{\rho c_j}}, \tag{33}$$

where

$$\widetilde{\rho c_n} = \max\big(0,\min(\rho,\rho c_n)\big), \tag{34}$$

and $(\rho c_n)^f$ is the adjusted species mass concentration. Equation (32) can also be enforced on the primitive mass fractions using

$$(c_n)^f = \frac{\widetilde{c_n}}{\sum_{j=1}^{N_s}\widetilde{c_j}}, \tag{35}$$

where

$$\widetilde{c_n} = \max\left(0, \min(1, c_n)\right), \tag{36}$$

and $(c_n)^f$ is the adjusted species mass concentration. Many different constraint techniques were tested over the course of this work. However, any technique for constraining species leads to violation of the conservation of species mass concentration. Therefore, it is best to minimize the necessity and application of these constraint techniques. Since numerical oscillations are responsible for the appearance of nonphysical species values, it is more beneficial to suppress numerical oscillations than to improve species constraint enforcement techniques.

4. Numerical oscillation reduction techniques

4.1. Overview

In previous research that utilizes Chord [24,38], the PPM limiter [5] sufficiently suppressed oscillations for flows with strong discontinuities. However, issues associated with numerical oscillations were observed when modeling reacting flows. In combination with the PPM limiter, new techniques are necessary. The techniques must have the following properties. First, the techniques must suppress oscillations in flow solutions that contain detonation waves. Ideally, the techniques would not increase the number of interior neighboring cells involved in the solution. Finally, the techniques must retain fourth-order accuracy in regions of smooth flow.

Accordingly, the following techniques have been devised, implemented, and tested:

- Face value limiting techniques
  - face value limiting (FVL)
  - primitive variable limiting selection
- DC limiting (DCL) techniques
  - cell- and face-based DC flattening
  - face construction order reduction (FCOR)

Subsequent sections will delineate the methodology and demonstrate the reduction of numerical oscillations on problems with shocks.

4.2. Face value limiting

While the base limiting approach that we use is the high-order extension to the PPM limiter recommended by McCorquodale and Colella [5], the original PPM limiter [39] can be viewed as three separate steps:

1. limit the face value interpolation;
2. limit the parabolic interpolant construction with consideration for smooth extrema;
3. apply slope flattening to the interpolants.

As recommended by McCorquodale and Colella, the first step is typically not applied to avoid excessive dissipation. However, our numerical experiments of flows with strong shock and detonation waves have shown that FVL appears to be necessary for multispecies or reacting flows. The FVL method developed in this research is based, in part, on the fourth-order face value limiting proposed by Colella and Sekora [4].

The remainder of this subsection provides the detailed methodology and a demonstration of improvements to the solution.

4.2.1. Methodology

The proposed FVL method replaces the fourth-order face interpolation in step S.5 in Section 3.2. A few terms are defined for the sake of improving readability of the method. The fourth-order, undivided second derivative at a face is calculated using

$$\left(\delta^2\phi\right)_{\boldsymbol{i}+\frac{1}{2}\boldsymbol{e}^d} = \left(\langle\phi\rangle_{\boldsymbol{i}+2\boldsymbol{e}^d} - \langle\phi\rangle_{\boldsymbol{i}+\boldsymbol{e}^d} - \langle\phi\rangle_{\boldsymbol{i}} + \langle\phi\rangle_{\boldsymbol{i}-\boldsymbol{e}^d}\right)/2\,. \tag{37}$$

The undivided third derivative at a face is calculated using

$$\left(\delta^3\phi\right)_{\boldsymbol{i}+\frac{1}{2}\boldsymbol{e}^d} = \left(\delta^2\phi\right)_{\boldsymbol{i}+\boldsymbol{e}^d} - \left(\delta^2\phi\right)_{\boldsymbol{i}}\,, \tag{38}$$

where

$$\left(\delta^2\phi\right)_{\boldsymbol{i}} = \langle\phi\rangle_{\boldsymbol{i}+\boldsymbol{e}^d} - 2\langle\phi\rangle_{\boldsymbol{i}} + \langle\phi\rangle_{\boldsymbol{i}-\boldsymbol{e}^d}\,. \tag{39}$$

The error in a cell is estimated using [10]

$$e_{\boldsymbol{i}} = \left|\frac{-\langle\phi\rangle_{\boldsymbol{i}-2\boldsymbol{e}^d} + 4\langle\phi\rangle_{\boldsymbol{i}-\boldsymbol{e}^d} + 4\langle\phi\rangle_{\boldsymbol{i}+\boldsymbol{e}^d} - \langle\phi\rangle_{\boldsymbol{i}+2\boldsymbol{e}^d}}{6\langle\phi\rangle_{\boldsymbol{i}}} - 1\right|. \tag{40}$$

The FVL methodology, applied at a face $\boldsymbol{i}+\frac{1}{2}\boldsymbol{e}^d$ for each primitive variable, is described by the following 4 steps:

1. Interpolate the fifth-order face value using

$$\langle\phi\rangle_{\boldsymbol{i}+\frac{1}{2}\boldsymbol{e}^d} = \frac{\langle\phi\rangle_{\boldsymbol{i}} + \langle\phi\rangle_{\boldsymbol{i}+\boldsymbol{e}^d}}{2} - \frac{\left(\delta^2\phi\right)_{\boldsymbol{i}-\frac{1}{2}\boldsymbol{e}^d} + 18\left(\delta^2\phi\right)_{\boldsymbol{i}+\frac{1}{2}\boldsymbol{e}^d} + \left(\delta^2\phi\right)_{\boldsymbol{i}+\frac{3}{2}\boldsymbol{e}^d}}{120}\,, \tag{41}$$

where the undivided second derivatives are computed using Eq. (37). Note that if $\left(\delta^2\phi\right)_{\boldsymbol{i}-\frac{1}{2}\boldsymbol{e}^d}$, $\left(\delta^2\phi\right)_{\boldsymbol{i}+\frac{1}{2}\boldsymbol{e}^d}$, and $\left(\delta^2\phi\right)_{\boldsymbol{i}+\frac{3}{2}\boldsymbol{e}^d}$ are all computed from a polynomial fit through $\langle\phi\rangle_{\boldsymbol{i}-\boldsymbol{e}^d}$, $\langle\phi\rangle_{\boldsymbol{i}}$, and $\langle\phi\rangle_{\boldsymbol{i}+\boldsymbol{e}^d}$, the standard fourth-order approximation [40] is recovered,

$$\langle\mathbf{W}\rangle_{\boldsymbol{i}+\frac{1}{2}\boldsymbol{e}^d} = \frac{-\langle\mathbf{W}\rangle_{\boldsymbol{i}-\boldsymbol{e}^d} + 7\langle\mathbf{W}\rangle_{\boldsymbol{i}} + 7\langle\mathbf{W}\rangle_{\boldsymbol{i}+\boldsymbol{e}^d} - \langle\mathbf{W}\rangle_{\boldsymbol{i}+2\boldsymbol{e}^d}}{12}\,. \tag{42}$$

2. If $\left(\langle\phi\rangle_{\boldsymbol{i}+\frac{1}{2}\boldsymbol{e}^d} - \langle\phi\rangle_{\boldsymbol{i}}\right)\left(\langle\phi\rangle_{\boldsymbol{i}+\boldsymbol{e}^d} - \langle\phi\rangle_{\boldsymbol{i}+\frac{1}{2}\boldsymbol{e}^d}\right) > 0$, then the face value is not a local extremum and FVL is not applied. Similarly, if $e_{\boldsymbol{i}} < 1\times10^{-3}$ and $e_{\boldsymbol{i}+\boldsymbol{e}^d} < 1\times10^{-3}$, then the values around the face are smooth and FVL is not applied; these tolerances come from Houim and Kuo [10]. Otherwise, continue to the next step.
3. Check that the interpolated face value is not a small perturbation of a cubic interpolation using

$$\alpha\max\left(\left|\left(\delta^3\phi\right)^{\min}_{\boldsymbol{i}+\frac{1}{2}\boldsymbol{e}^d}\right|, \left|\left(\delta^3\phi\right)^{\max}_{\boldsymbol{i}+\frac{1}{2}\boldsymbol{e}^d}\right|\right) \leq \left(\delta^3\phi\right)^{\max}_{\boldsymbol{i}+\frac{1}{2}\boldsymbol{e}^d} - \left(\delta^3\phi\right)^{\min}_{\boldsymbol{i}+\frac{1}{2}\boldsymbol{e}^d}\,, \tag{43}$$

where $\alpha = 0.1$ (from McCorquodale and Colella [5]),

$$\left(\delta^3\phi\right)^{\min}_{\boldsymbol{i}+\frac{1}{2}\boldsymbol{e}^d} = \min\left(\left(\delta^3\phi\right)_{\boldsymbol{i}+\frac{1}{2}\boldsymbol{e}^d}, \left(\delta^3\phi\right)_{\boldsymbol{i}-\frac{1}{2}\boldsymbol{e}^d}, \left(\delta^3\phi\right)_{\boldsymbol{i}+\frac{3}{2}\boldsymbol{e}^d}\right), \tag{44}$$

and

$$\left(\delta^3\phi\right)^{\max}_{\boldsymbol{i}+\frac{1}{2}\boldsymbol{e}^d} = \max\left(\left(\delta^3\phi\right)_{\boldsymbol{i}+\frac{1}{2}\boldsymbol{e}^d}, \left(\delta^3\phi\right)_{\boldsymbol{i}-\frac{1}{2}\boldsymbol{e}^d}, \left(\delta^3\phi\right)_{\boldsymbol{i}+\frac{3}{2}\boldsymbol{e}^d}\right). \tag{45}$$

If Eq. (43) is false, do not apply any FVL. Otherwise, continue to the next step. This test is similar to one used by McCorquodale and Colella [5].
4. Set the face value based on the undivided first derivative to the left and right of the face using

$$(\delta\phi)^L = \langle\phi\rangle_{\boldsymbol{i}+\boldsymbol{e}^d} - \langle\phi\rangle_{\boldsymbol{i}} - \left(\delta^2\phi\right)_{\boldsymbol{i}+\frac{1}{2}\boldsymbol{e}^d}\,, \tag{46}$$

and

$$(\delta\phi)^R = \langle\phi\rangle_{\boldsymbol{i}+\boldsymbol{e}^d} - \langle\phi\rangle_{\boldsymbol{i}} + \left(\delta^2\phi\right)_{\boldsymbol{i}+\frac{1}{2}\boldsymbol{e}^d}\,, \tag{47}$$

respectively. If the derivatives change signs, set the face value to a linear average of the adjacent cells. Otherwise, check the magnitudes of the derivatives. If the derivative on one side of the face is three times the derivative on the other side of the face, fit a quadratic through both cells that ensures the smaller derivative becomes zero. This can be shown in equation form as

$$\langle\phi\rangle_{\boldsymbol{i}+\frac{1}{2}\boldsymbol{e}^d} = \frac{\langle\phi\rangle_{\boldsymbol{i}} + \langle\phi\rangle_{\boldsymbol{i}+\boldsymbol{e}^d}}{2} - \frac{1}{6}\begin{cases} 0, & \text{if } (\delta\phi)^L(\delta\phi)^R < 0\,,\\ \langle\phi\rangle_{\boldsymbol{i}} - \langle\phi\rangle_{\boldsymbol{i}+\boldsymbol{e}^d}, & \text{if } |(\delta\phi)^L| > 3|(\delta\phi)^R|\,,\\ \langle\phi\rangle_{\boldsymbol{i}+\boldsymbol{e}^d} - \langle\phi\rangle_{\boldsymbol{i}}, & \text{if } |(\delta\phi)^R| > 3|(\delta\phi)^L|\,,\\ \left(\delta^2\phi\right)_{\boldsymbol{i}+\frac{1}{2}\boldsymbol{e}^d}, & \text{otherwise}\,. \end{cases} \tag{48}$$

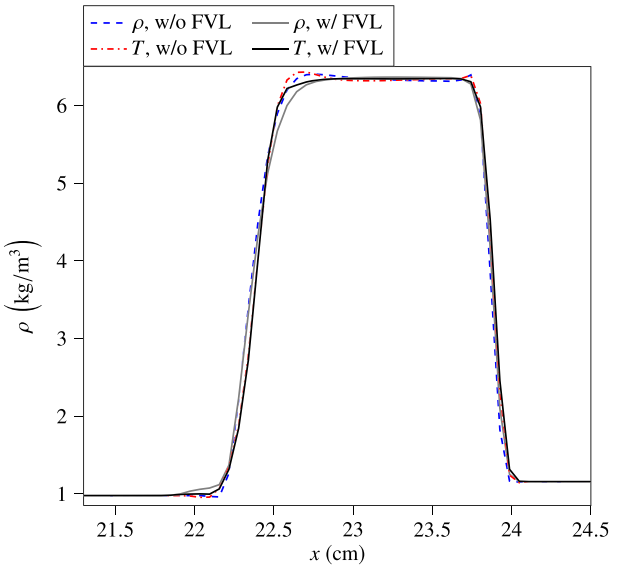

Fig. 1. Density profiles of the shock (right) and contact surface (left) at solution time $t = 49$ μs. The blue dashed line: density is interpolated and FVL is not applied; red dash-dot line: temperature is interpolated and FVL is not applied; gray line: density is interpolated and FVL is applied; black line: temperature is interpolated and FVL is applied. Pressure is always interpolated/limited. (For interpretation of the colors in the figure(s), the reader is referred to the web version of this article.)

4.2.2. Demonstration

A shock tube case with a shock strength of Ma ≈ 4.9 is used to demonstrate the capability of the FVL method and impact of the selection of primitive variable to calculate using the ideal gas law. The shock tube domain is $L_x \times L_y = 31.25$ cm $\times$ 0.4883 cm, and the initial discontinuity is at $x = 15.625$ cm. The mesh is $N_x \times N_y = 512 \times 8$. The domain is periodic in the y-direction, and the x-direction boundary conditions are slip walls. Half of the shock tube is composed of air and the other half is composed of helium. A large gradient of the mixture gas constants form at the initial discontinuity due to disparate molecular weights of He and O_2/N_2. The shock tube is initialized with the following left and right properties, denoted by subscripts L and R, respectively,

$$\left(p, T, c_{N_2}, c_{O_2}, c_{He}\right)_L = \left(7.20 \times 10^6 \text{ Pa}, 2 \times 10^3 \text{ K}, 0, 0, 1\right)$$
$$\left(p, T, c_{N_2}, c_{O_2}, c_{He}\right)_R = \left(1 \times 10^5 \text{ Pa}, 300 \text{ K}, 0.767, 0.233, 0\right).$$

It is worth mentioning that, through numerical experiments, we found that the severity of numerical oscillations in the solution depend on which primitive variables are interpolated/limited and which are calculated at a face. If all three variables (ρ, p, and T) are interpolated independently, the state on the face violates the ideal gas law. Therefore, only two variables can be interpolated, and the third must be calculated from the ideal gas law. Shock tube tests run as part of this work demonstrated that pressure must always be interpolated/limited to obtain a solution.

Four different solutions are shown in Figs. 1 and 2. In the figures, "w/ FVL" denotes FVL is applied and "w/o FVL" denotes that FVL is not applied. Also, the variable shown in the legend denotes the variable that is interpolated/limited. The density profiles in Fig. 1 show that the overshoot at the contact surface is eliminated when FVL is applied. Since temperature is a function of density, energy, and mass fractions, the temperature profiles in Fig. 2 demonstrate more severe numerical oscillations than the density profiles. As in the profiles of density, numerical oscillations arise around the contact surface. Oscillations around the contact surface are eliminated when temperature is interpolated and density is calculated using the ideal gas law. The implication from these results is that the least oscillatory scheme is obtained when applying all three steps in the PPM limiter, with the new technique described in Section 4.2.1 used as step 1, to all primitive states except density, which is calculated using the ideal gas law. Chord solutions shown beyond this point are obtained by interpolating/limiting temperature and pressure, solving for density at the face, and applying FVL, unless otherwise specified.

It is insightful to assess the performance of the FVL method by comparing with other limiting techniques for thermally-perfect, multispecies flows with strong discontinuities, such as the family of WENO limiting schemes. Specifically, the WENO-Z limiter is investigated with the PeleC code [41] using the shock tube problem. Details regarding this limiter are provided by Motheau et al. [42]. Both Chord and PeleC are compressible FVM solvers; the latter is not globally fourth-order accurate and does not explicitly enforce the physical constraints in Eq. (32), potentially leading to

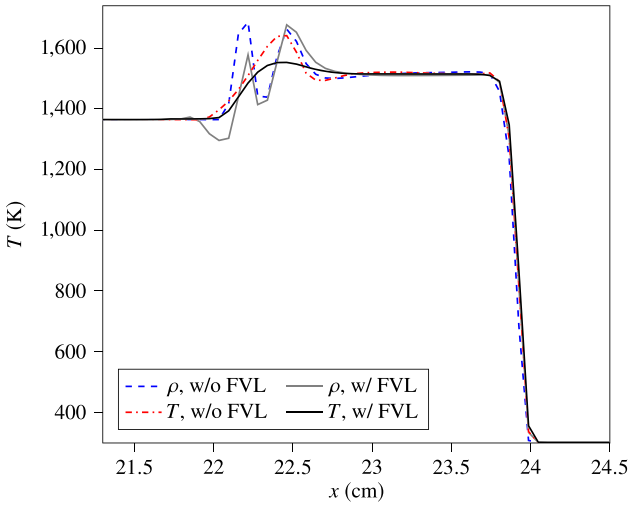

Fig. 2. Temperature profiles of the shock (right) and contact surface (left) at solution time $t = 49$ µs. The blue dashed line: density is interpolated and FVL is not applied; red dash-dot line: temperature is interpolated and FVL is not applied; gray line: density is interpolated and FVL is applied; black line: temperature is interpolated and FVL is applied. Pressure is always interpolated/limited.

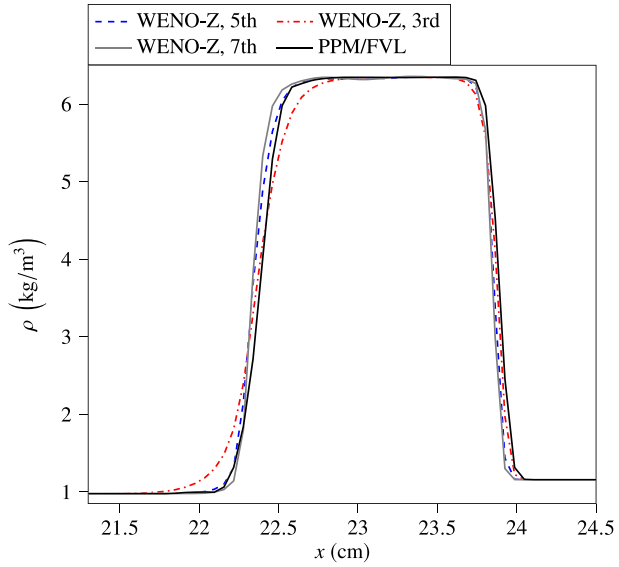

Fig. 3. Density profiles of the shock (right) and contact surface (left) at solution time $t = 49$ µs. The blue dashed line: PeleC solution using the fifth-order WENO-Z limiter; red dash-dot line: PeleC solution using the third-order WENO-Z limiter; gray line: PeleC solution using the seventh-order WENO-Z limiter; black line: Chord solution using the PPM limiter with FVL.

$$\rho \neq \sum_{n=1}^{N_s} \rho c_n \,. \tag{49}$$

To ensure the comparisons are reasonable, the WENO-Z solutions also use temperature-based limiting.

Figs. 3 and 4 show the density and temperature profiles, respectively, to compare the WENO-Z limiting schemes in PeleC with the PPM/FVL in Chord. The density profiles in Fig. 3 show the third-order WENO-Z scheme introduces dissipation around the contact surface. The PPM/FVL solution is slightly more dissipative than the fifth and seventh-order WENO-Z but less dissipative than the third-order WENO-Z. There is more variability between the temperature profiles in Fig. 4. All three WENO-Z solutions have an undershoot prior to the contact surface followed by an overshoot at the contact surface; this overshoot is sharp for the fifth and seventh-order schemes. In contrast, this sharp overshoot at the contact surface is eliminated in the Chord solution. The results in Figs. 3 and 4 suggest that the PPM/FVL scheme suppresses severe oscillations near discontinuities more than the low-dissipation WENO-Z schemes for thermally-perfect, multispecies flows.

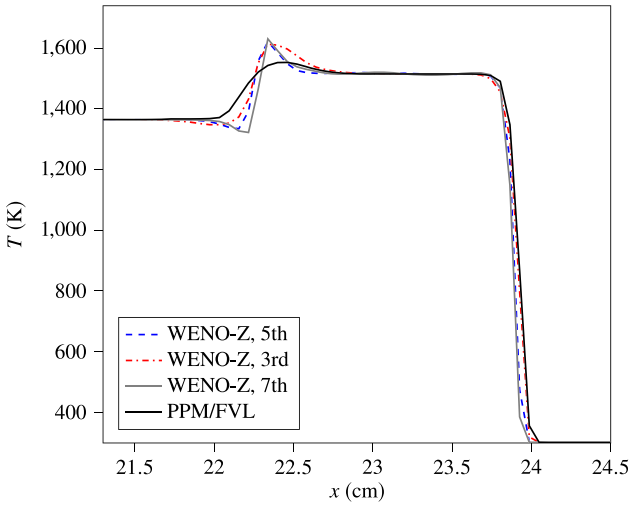

Fig. 4. Temperature profiles of the shock (right) and contact surface (left) at solution time $t = 49$ µs. The blue dashed line: PeleC solution using the fifth-order WENO-Z limiter; red dash-dot line: PeleC solution using the third-order WENO-Z limiter; gray line: PeleC solution using the seventh-order WENO-Z limiter; black line: Chord solution using the PPM limiter with FVL.

4.3. Deconvolution/convolution limiting

Existing limiting techniques for FVMs [5,35,36] focus on reducing oscillations at the faces through means such as interpolant limiting and slope flattening. These existing techniques are often sufficient for second-order FVMs, where the cell and flux integrals are approximated using the midpoint rule, and for fourth-order solutions of calorically-perfect gases. As previously mentioned, the finite-difference approximation of the derivatives require information from neighboring cells or faces. Near large gradients or discontinuous regions, these numerical approximations can introduce severe, nonphysical oscillations into the flow. Furthermore, the impact of these nonphysical oscillations can be exacerbated by the nonlinearities of the thermodynamic system. To give a relevant scenario (coming from our many observations), assume that severe oscillations are introduced during the deconvolution of $\langle \mathbf{U} \rangle_{\boldsymbol{i}}$ in Eq. (22). An algorithm would traditionally rely on face limiting or slope flattening mechanisms to eliminate these oscillations. However, due to the issues detailed in Section 3.3, these oscillations must be addressed before limiting or flattening face values.

Additionally, the PPM face and cell-interpolant limiting and slope flattening are unable to eliminate oscillations introduced during the face-based DC operations due to the order of operations. Unfortunately, literature regarding techniques to alleviate such oscillations in high-order FVMs [43] is scarce. Therefore, it is our hope that the DCL techniques developed and tested in the present research will help resolve these issues and contribute to the literature in this particular context.

4.3.1. Methodology: deconvolution/convolution flattening

The DC flattening technique selectively reduces the order of accuracy of the DC operations based on the normalized difference between the fourth-order and second-order approximation of a variable. The normalized difference is calculated using

$$(\Delta\phi)^{\mathrm{DC}} = \frac{\left|\phi^{(2)} - \phi^{(4)}\right|}{C_1 + \left|\phi^{(2)}\right|}, \tag{50}$$

where the constant C_1 is 1×10^{-20} to prevent the denominator from going to zero. The DC flattening coefficient is then solved as

$$\eta^{\mathrm{DC}} = \begin{cases} 0, & \text{if } (\Delta\phi)^{\mathrm{DC}} > \epsilon^{\mathrm{DC}}, \\ 1, & \text{otherwise}, \end{cases} \tag{51}$$

where $\epsilon^{\mathrm{DC}} = 0.2$ is the tolerance for the DC order reduction. The value of ϵ^{DC} is determined from numerical experimentation. The tolerance ϵ^{DC} tolerance represents a trade-off between accuracy and numerical oscillations. Generally, the lower the tolerance, the greater the reduction in oscillations at the cost of decreased accuracy. The DC flattening coefficient is applied using

$$\phi^{\mathrm{F}} = (1 - \eta^{\mathrm{DC}})\phi^{(2)} + \eta^{\mathrm{DC}}\phi^{(4)}, \tag{52}$$

where ϕ^{F} represents the final flattened value in a cell or at a face. If the nonlinear solution in Eq. (30) fails to converge to a solution, the values for T and p are set to 1.2×10^{300} so that $(\Delta\phi)^{\mathrm{DC}} \approx 1 > \epsilon^{\mathrm{DC}}$. This ensures the order of accuracy is dropped when the nonlinear solution fails to converge.

Regarding Eq. (50), special care must be taken when velocity values approach zero. To address this issue, the constant $C_1 = 1$ when $\phi = \boldsymbol{u}$. Special care must also be taken when applying DC flattening to values that are less than one, like mass fractions. To address this issue, the solution of Eq. (50) when $\phi = c_n, \forall n \in N_s$ is

$$(\Delta\phi)^{\mathrm{DC}} = \frac{\left|\phi^{(2)} - \phi^{(4)}\right|}{C_1 + \left|\phi^{(2)}\right| + \left|\phi^{(4)}\right|}. \tag{53}$$

4.3.2. Methodology: face construction order reduction

In addition to DC flattening, it is necessary to selectively modify the order of accuracy of the values used during the construction and limiting of face values. Three different checks are required to see if FCOR is necessary. The first check at the $\boldsymbol{i} + \frac{1}{2}\boldsymbol{e}^d$ face involves the percent difference between the linear face construction using fourth-order average values and second-order values and is given by

$$\phi^{\max}_{\boldsymbol{i}+\frac{1}{2}\boldsymbol{e}^d}\epsilon_1^{\mathrm{FR}} < \left(\phi^{\max}_{\boldsymbol{i}+\frac{1}{2}\boldsymbol{e}^d} - \phi^{\min}_{\boldsymbol{i}+\frac{1}{2}\boldsymbol{e}^d}\right), \tag{54}$$

where $\epsilon_1^{\mathrm{FR}} = 1 \times 10^{-3}$,

$$\phi^{\max}_{\boldsymbol{i}+\frac{1}{2}\boldsymbol{e}^d} = \frac{1}{2}\max\left(\left|\phi^{(2)}_{\boldsymbol{i}+\boldsymbol{e}^d} + \phi^{(2)}_{\boldsymbol{i}}\right|, \left|\phi^{(4)}_{\boldsymbol{i}+\boldsymbol{e}^d} + \phi^{(4)}_{\boldsymbol{i}}\right|\right), \tag{55}$$

and

$$\phi^{\min}_{\boldsymbol{i}+\frac{1}{2}\boldsymbol{e}^d} = \frac{1}{2}\min\left(\left|\phi^{(2)}_{\boldsymbol{i}+\boldsymbol{e}^d} + \phi^{(2)}_{\boldsymbol{i}}\right|, \left|\phi^{(4)}_{\boldsymbol{i}+\boldsymbol{e}^d} + \phi^{(4)}_{\boldsymbol{i}}\right|\right). \tag{56}$$

The second check evaluates the normalized difference between the undivided, second-order face derivatives. The second check at the $\boldsymbol{i} + \frac{1}{2}\boldsymbol{e}^d$ face is

$$\delta^{1,\max}\epsilon_2^{\mathrm{FR}} < \left|\delta^1\left(\phi^{(2)}\right) - \delta^1\left(\phi^{(4)}\right)\right|, \tag{57}$$

where $\epsilon_2^{\mathrm{FR}} = 1 \times 10^{-3}$, the second-order, first derivative on the face is calculated using

$$\delta^1(\phi) = \phi_{\boldsymbol{i}+\boldsymbol{e}^d} - \phi_{\boldsymbol{i}}, \tag{58}$$

and

$$\delta^{1,\max} = \max\left(\left|\delta^1\left(\phi^{(2)}\right)\right|, \left|\delta^1\left(\phi^{(4)}\right)\right|\right). \tag{59}$$

The tolerances for both tests are determined through numerical experimentation conducted as part of this research. As with the DC flattening, the lower tolerances generally result in greater reduction of oscillations at the cost of decreased accuracy. The final check comes from the tolerance check for the Brent's nonlinear solver. It is performed to ensure FCOR is not applied in regions where round-off error becomes significant. This test is

$$\delta^{1,\max} > \left(4\epsilon_1\phi^{\max}_{\boldsymbol{i}+\frac{1}{2}\boldsymbol{e}^d} + \epsilon_2\right), \tag{60}$$

where the tolerances for ϵ_1 and ϵ_2 come from Eq. (31). If Eqs. (54), (57), and (60) are all true, then the face values are constructed using the second-order, primitive state.

4.3.3. Implementation

Implementing the DCL techniques requires modifying the standard solution procedure described in Section 3.2.

- After step S.4, the DC flattening coefficient is calculated using the normalized difference of

$$\left(\Delta\langle\widetilde{\mathbf{W}}\rangle\right)^{\mathrm{DC}} = \frac{\left|\widetilde{\mathbf{W}}|_{(2)} - \langle\widetilde{\mathbf{W}}\rangle\right|}{C_1 + \left|\widetilde{\mathbf{W}}|_{(2)}\right|}. \tag{61}$$

  The DC flattening coefficient is applied using

$$\langle\widetilde{\mathbf{W}}\rangle^{\mathrm{F}} = (1 - \eta^{\mathrm{DC}})\widetilde{\mathbf{W}}|_{(2)} + \eta^{\mathrm{DC}}\langle\widetilde{\mathbf{W}}\rangle, \tag{62}$$

  where $\langle\widetilde{\mathbf{W}}\rangle_{\boldsymbol{i}}$ is replaced by $\langle\widetilde{\mathbf{W}}\rangle^{\mathrm{F}}_{\boldsymbol{i}}$ throughout the remainder of the solution procedure in Section 3.2. This step is then repeated for the cell-centered nonnative primitive state, $\widetilde{\mathbf{W}}$.

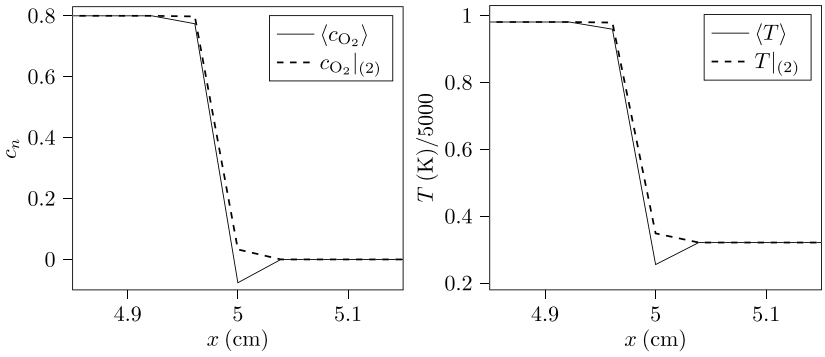

(a) Oxygen mass fraction profile. **(b)** Normalized temperature profile.

Fig. 5. Demonstration of oscillations produced during solution procedure. The solid, black lines are the fourth-order, cell-averaged values and the dashed, black lines are the second-order, cell-averaged values.

- If Eqs. (54), (57), (60) are all true (where $\phi_{\boldsymbol{i}}^{(2)} \rightarrow \left(\widetilde{\mathbf{W}}|_{(2)}\right)_{\boldsymbol{i}}$ from Eq. (21) and $\phi_{\boldsymbol{i}}^{(4)} \rightarrow \langle \widetilde{\mathbf{W}} \rangle_{\boldsymbol{i}}$ from Eq. (24)), then the FVL technique in Section 4.2 uses $(\widetilde{\mathbf{W}}|_{(2)})_{\boldsymbol{i}}$ instead of $\langle \widetilde{\mathbf{W}} \rangle_{\boldsymbol{i}}$ in Eqs. (41) and (48).
- Following the solution of the nonnative primitive state on the faces in step S.11, the DC flattening is applied to the following:
  - Compute a new value of η^{DC} using Eqs. (50) and (51) where $\phi^{(2)} \rightarrow \langle \mathbf{W} \rangle_{\boldsymbol{i}+\frac{1}{2}\boldsymbol{e}^d}$, $\phi^{(4)} \rightarrow \mathbf{W}_{\boldsymbol{i}+\frac{1}{2}\boldsymbol{e}^d}$, and $\mathbf{W}_{\boldsymbol{i}+\frac{1}{2}\boldsymbol{e}^d}$ is replaced with $\mathbf{W}^{\mathrm{F}}_{\boldsymbol{i}+\frac{1}{2}\boldsymbol{e}^d}$ from Eq. (52) for the remainder of the solution procedure.
  - Repeat the last step except $\phi^{(2)} \rightarrow \left(T|_{(2)}\right)_{\boldsymbol{i}+\frac{1}{2}\boldsymbol{e}^d}$ from Eq. (25), $\phi^{(4)} \rightarrow T_{\boldsymbol{i}+\frac{1}{2}\boldsymbol{e}^d}$ from Eq. (26), and $T_{\boldsymbol{i}+\frac{1}{2}\boldsymbol{e}^d}$ is replaced with $T^{\mathrm{F}}_{\boldsymbol{i}+\frac{1}{2}\boldsymbol{e}^d}$ from Eq. (52) for the remainder of the solution procedure.
  - Repeat the last step except $\phi^{(2)} \rightarrow \left(T|_{(2)}\right)_{\boldsymbol{i}+\frac{1}{2}\boldsymbol{e}^d}$ from Eq. (25), $\phi^{(4)} \rightarrow T_{\boldsymbol{i}+\frac{1}{2}\boldsymbol{e}^d}$ from Eq. (27), and $\langle T \rangle_{\boldsymbol{i}+\frac{1}{2}\boldsymbol{e}^d}$ is replaced with $\langle T \rangle^{\mathrm{F}}_{\boldsymbol{i}+\frac{1}{2}\boldsymbol{e}^d}$ from Eq. (52) for the remainder of the solution procedure.

4.3.4. Demonstration: deconvolution/convolution flattening

A shock tube problem demonstrates the numerical oscillations that occur due to the DC operations near large gradients. The shock tube domain is $L_x \times L_y = 10$ cm $\times$ 0.625 cm, and the initial discontinuity is at $x = 5$ cm. The mesh is $N_x \times N_y = 128 \times 8$ cells with two refined levels, each with a refinement ratio of 2. Refinement is based on gradients of density. This shock tube problem differs from the one in Section 4.2 because each case is deliberately designed to expose different issues. The initial left and right states in the shock tube are given as

$$\left(p, T, c_{N_2}, c_{O_2}, c_{CO}, c_{CO_2}\right)_L = \left(1.177 \times 10^6 \text{ Pa}, 4.905 \times 10^3 \text{ K}, 0.1, 0.8, 0, 0.1\right)$$
$$\left(p, T, c_{N_2}, c_{O_2}, c_{CO}, c_{CO_2}\right)_R = \left(1. \times 10^5 \text{ Pa}, 1.607 \times 10^3 \text{ K}, 0.5, 0, 0.25, 0.25\right).$$

Fig. 5 shows the profiles of c_{O_2} and the normalized temperature on the first refined mesh level during the first time step. The dashed, black line is the solution of Eq. (21) and the solid, gray line is the solution of Eq. (24). Fig. 5a shows a nonphysical, negative cell-averaged mass fraction at the discontinuity. Fig. 5b shows the cell-averaged temperature is 1278 K at $x = 5$ cm, while the second-order, cell-averaged temperature is 1744 K; this produces a value of $(\Delta T)^{\mathrm{DC}} = 0.26$ from Eq. (50). If c_{CO} is replaced with c_{H_2} in the initialization, the oscillations introduced during deconvolution cause the nonlinear solution for the cell-centered temperature to diverge during the first time step. The DC flattening technique would reduce the order of the DC operations at this discontinuity and eliminate the oscillations in Fig. 5.

4.3.5. Demonstration: face construction order reduction

An ODW over a wedge is used to demonstrate the improvements provided by the FCOR technique. Fig. 6 depicts the basic structure of an ODW over a wedge. In the figure, a reactive mixture moving at a high Mach number encounters a wedge, causing an oblique shock to form. The heating from the oblique shock induces deflagration and ultimately produces a detonation wave. In the present work, a Schwarz-Christoffel mapping transformation [44] is used to model the wedge, as illustrated in Fig. 7, where l_r represents the length of the ramp and l_s represents the length of the lead up to the ramp.

For the current problem, $\theta = 23.8°$, $\mathrm{Ma}_\infty = 8$, $p_\infty = 34$ kPa, and $T_\infty = 300$ K. The mixture is a stoichiometric mixture of hydrogen and air. The current setup is based on a case run by Figueria da Silva and Deshaies [45] except the reaction

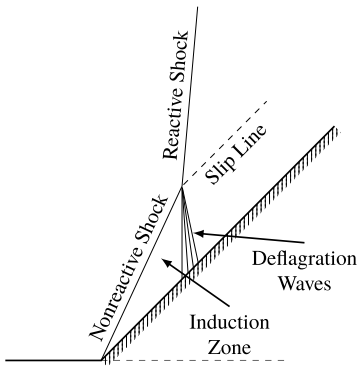

Fig. 6. Schematic of the basic structure of an ODW over a wedge.

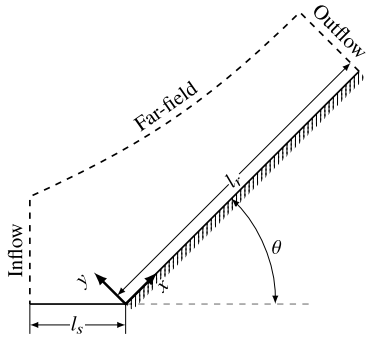

Fig. 7. Demonstration of the computational domain for the wedge geometry.

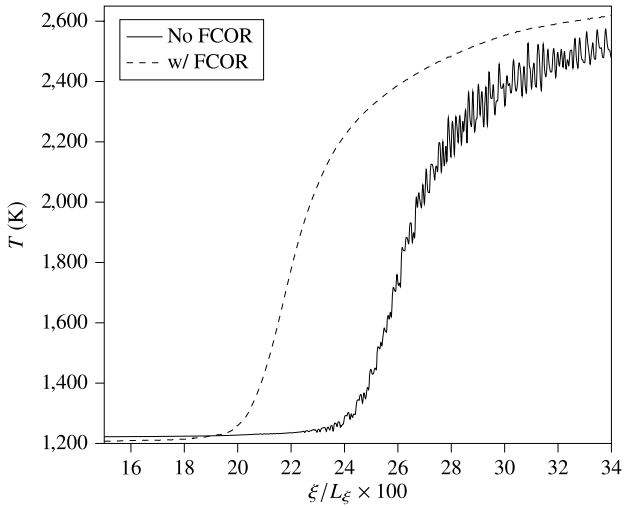

Fig. 8. ODW temperature profiles extracted in computational space at solution time $t = 11.2$ µs. The profile is at a constant value of $\eta = 3 \times 10^{-4}$.

mechanism is the 9 species, 19-step mechanism from Billet et al. [46]. The lengths of the ramp and lead up to the ramp are $l_r = 7$ cm and $l_s = 0.5$ cm, respectively. The base mesh is 320×128, and the computational domain lengths are $L_\xi \times L_\eta = 1 \times 0.4$. The mesh has three additionally refined levels; the first two levels have refinement ratios of 4 and the third level has a refinement ratio of 2. Refinement is based on gradients of temperature, and there is fixed refinement in the layer of cells adjacent to the wall.

Fig. 8 shows temperature profiles taken along the direction of the lower boundary in the rectangular computational domain at a fixed point of $\eta = 3 \times 10^{-4}$, or 0.075% of the domain in the wall normal direction; this location represents the top of the numerical overheat region and at solution time $t = 11.2$ µs. The profiles show the temperature far behind the oblique shock wave (OSW), which forms at $\xi/L_\xi \times 100 \approx 4.9$. The rise in temperature is due to the heat release from

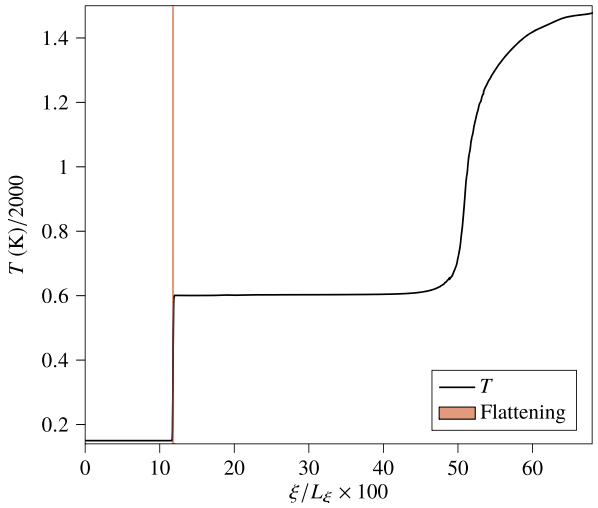

(a) Temperature profile of nonreactive shock and deflagration wave.

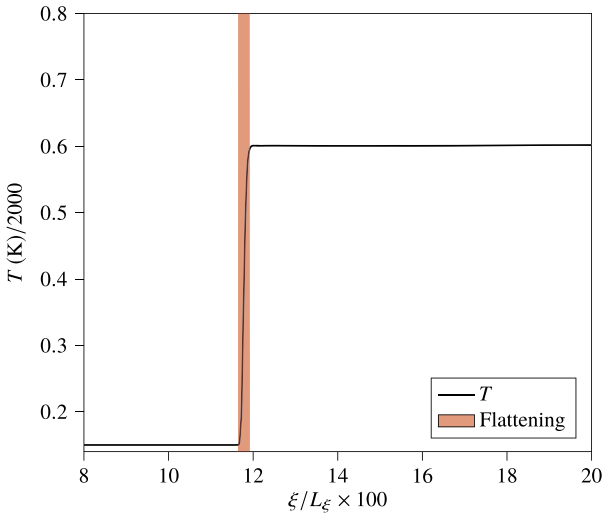

(b) Magnified temperature profile of nonreactive shock.

Fig. 9. ODW temperature profiles extracted in computational space at solution time $t = 22.1$ µs. The profiles are at a constant value of $\eta = 0.01$.

the reactions which are initiated due to the numerical overheating at the wall [47]. More information regarding ODWs and numerical overheating is provided in Section 5. Two different profiles are shown, the dashed line is the solution with FCOR applied, and the solid line is the solution without FCOR applied. Both solutions utilize FVL and DC flattening. The solution without FCOR contains severe oscillations as heat release occurs. These oscillations cause the solution to diverge shortly after the solution time $t = 11.2$ µs. The heat release locations between the solutions with and without FCOR differ by approximately 4% of the computational domain length. However, the oscillations are eliminated when the FCOR is utilized. In fact, FCOR is applied where the heat release induced by the numerical overheat at the wall interacts with the flow in the induction zone. Incurring increased overheating near the wall to reduce severe oscillations in the flow is deemed an acceptable trade-off to solve problems involving hypersonic flows with chemical reactions.

Figs. 9a and 9b show temperature profiles taken along the direction of the lower boundary in the rectangular computational domain at a fixed point of $\eta = 0.01$. The profiles are taken at solution time $t = 22.1$ µs. The figures use a red box to show locations where DC flattening and/or FCOR have reduced the order of accuracy of temperature during the stages of the latest time step. Fig. 9a shows the temperature profile from the nonreactive shock (the sharp rise at the left) to the heat release at the deflagration wave (the gradual rise at the right). Fig. 9b is a magnified view of Fig. 9a at the nonreactive shock. Since deflagration is a smooth phenomenon, we want to retain high-order accuracy in this region. However, we desire

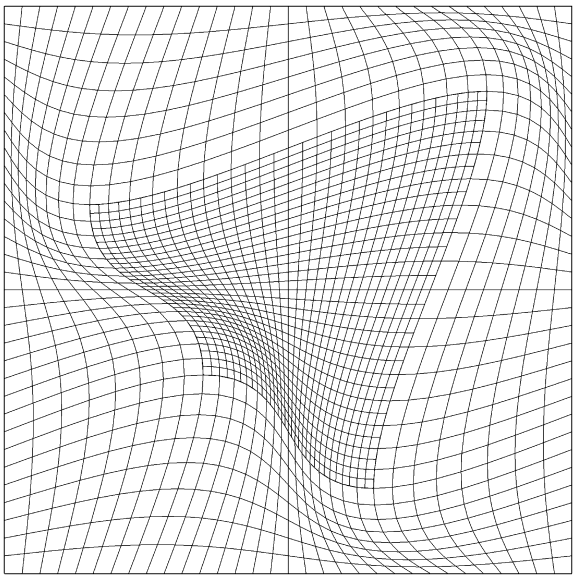

Fig. 10. Demonstration of a warped mesh with a single refined level where $\vec{S} = (0.1, 0.1)$.

order reduction around the nonreactive shock to eliminate or mitigate the formation of numerical oscillations. Both figures show that the DCL tests are properly calibrated to reduce the order near the shock but not in the region of deflagration.

5. Results

The limiting techniques presented in this work are tested and compared on a series of cases. First, the order of accuracy of the scheme is verified using a shear problem. Next, a shock tube problem is used to demonstrate the improvements provided by the techniques to the conservation of species mass concentrations. The calorically-perfect Shu-Osher and double Mach reflection problems are used to demonstrate the impact that the techniques have on discontinuities and small scale structures. Finally, the techniques are applied to solve a set of ODW problems. Other test cases, such as a mass diffusion bubble, were used for verification and validation but are not shown here for the sake of brevity. Previous work provides more details about some of these cases [22–24].

5.1. Order of accuracy verification

Algorithm accuracy is verified by examining the solution errors. Errors are measured with the L_∞-, L_1-, and L_2-norms of the difference between the "exact" solution and the numerical solution. The "exact" solution is analytically computed, if possible, or determined using Richardson extrapolation. The order of accuracy n, as in $\mathcal{O}(\Delta\xi^n)$, is defined by

$$n = \log\left(\frac{L_m(r\Delta\xi)}{L_m(\Delta\xi)}\right) / \log(r)\,, \tag{63}$$

where $L_m(\Delta\xi)$ is the m-norm of the error from a solution with a mesh of resolution $\Delta\xi$, and r is the refinement ratio between the meshes. For the verification in the present study, $r = 2$.

Richardson extrapolation is performed to project a more accurate solution based on the numerical solutions obtained at different spatial resolutions. More information regarding order of accuracy verification with Richardson extrapolation is provided by Guzik et al. [21]. For convenience, acronyms are used to denote mesh types. "PC" stands for the precoarse mesh, "C" for coarse, "M" for medium, "F" for fine, and "PF" for postfine. The convergence rates between two adjacent meshes are denoted as "PC-C", "C-M", etc. The PF solution is used to extrapolate an "exact" solution for a coarser grid solution.

Order of accuracy verification using a shear problem is a stringent test of transverse terms in the algorithm and uncovers many issues related to accuracy. Other verification test cases (such as a Gaussian acoustic pulse and mass diffusion bubble) were performed but are not shown here for the sake of brevity. The domain length is $L_x \times L_y = 1\ \text{m} \times 1\ \text{m}$ with all periodic boundaries and diffusion is neglected. The domain is initialized to a uniform pressure and temperature of $p = 1$ atm and $T = 300$ K, respectively. The initial fluid is comprised of mass fractions $c_{O_2} = 0.233$ and $c_{N_2} = 0.767$. The velocity is initialized using

$$u(x, y) = 100\cos(2\pi y)\,,\ v(x, y) = 100\cos(2\pi x)\,. \tag{64}$$

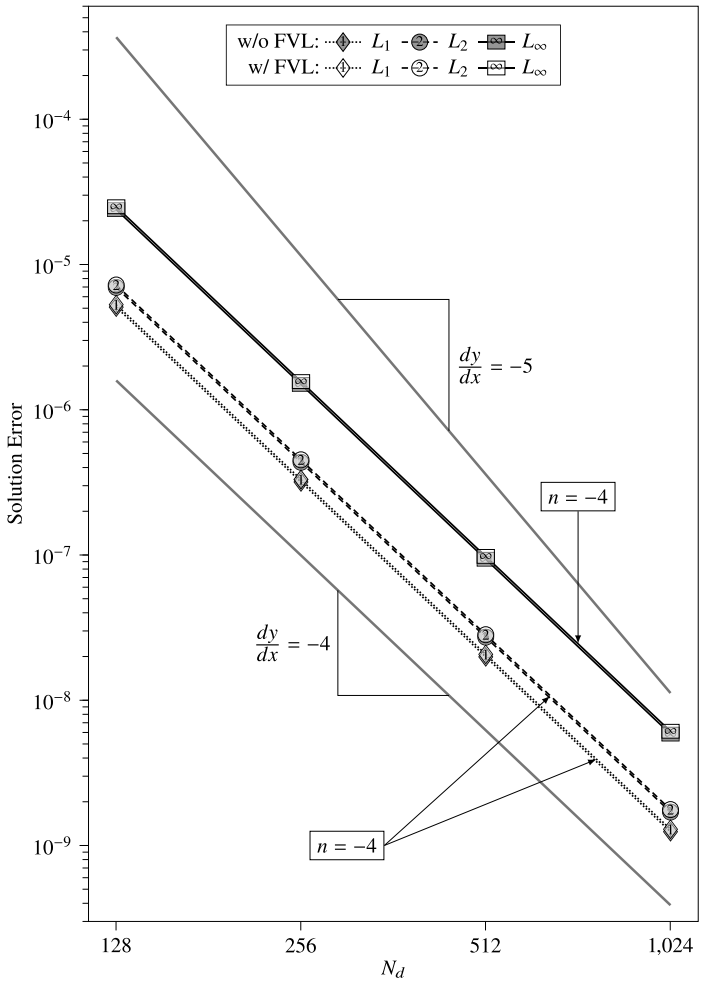

Fig. 11. Shear problem solution accuracy of x-momentum both without and with face value limiting, labeled "w/o FVL" and "w/ FVL", respectively.

In order to verify that the techniques work with curvilinear coordinate transformation, the shear problem uses a mesh that is warped according to

$$x_d = \xi_d + S_d \prod_{p=1}^{D} \sin\left(\frac{2\pi\xi_p}{L_p}\right),\ d = 1, \ldots, D\,, \tag{65}$$

where $\vec{L}$ is the length of the domain and $\vec{S}$ is a scaling factor that must be bounded by $0 \leq 2\pi S_d \leq L_d$ to ensure the mesh does not tangle. The scaling factor for the shear problem is $S_d = 0.1$. When AMR is used in the solution, the grid on the finer level is fixed in computational space from $(0.25, 0.25)$ to $(0.75, 0.75)$ with a refinement ratio between levels of 2. The refined level is placed so that large gradients occur at AMR interfaces. The warped mapping and refinement are illustrated in Fig. 10. More information regarding this specific mapping is provided by Colella et al. [48].

The solution accuracy of $\langle J\rho u\rangle$ is measured at solution time $t = 44.8$ µs and plotted in Figs. 11, 12, and 13. The PF mesh has 2048^2 cells, and the refinement ratios between the meshes is 2. Fig. 11 compares the solution accuracy between single-level solutions with and without FVL. The impact of FVL on the solution error is negligible. Fourth-order accuracy is achieved for all grids and solution norms. Fig. 12 compares the solution accuracy between solutions on single-level grids and solutions with one additional AMR level with neither solution using FVL. The resolution of the finest level of each AMR grid matches the resolution of the corresponding single-level grid. The error from the solution with one additionally refined level is larger than the error from the single-level solution. As described by Guzik et al. [21], a loss of up to one-order of accuracy can occur in coarse cells adjacent to the interfaces between coarse and fine levels; this impact is made more apparent when the interface is exposed to strong gradients. The order of accuracy of the L_1- and L_2-norms converges to approximately 3.95, while the L_∞-norm continues to increase from 3.5 to 3.82 as the grid is refined. Fig. 13 shows the same data as Fig. 12 except both solutions use FVL. The order of accuracy of the L_1- and L_2-norms begin to converge

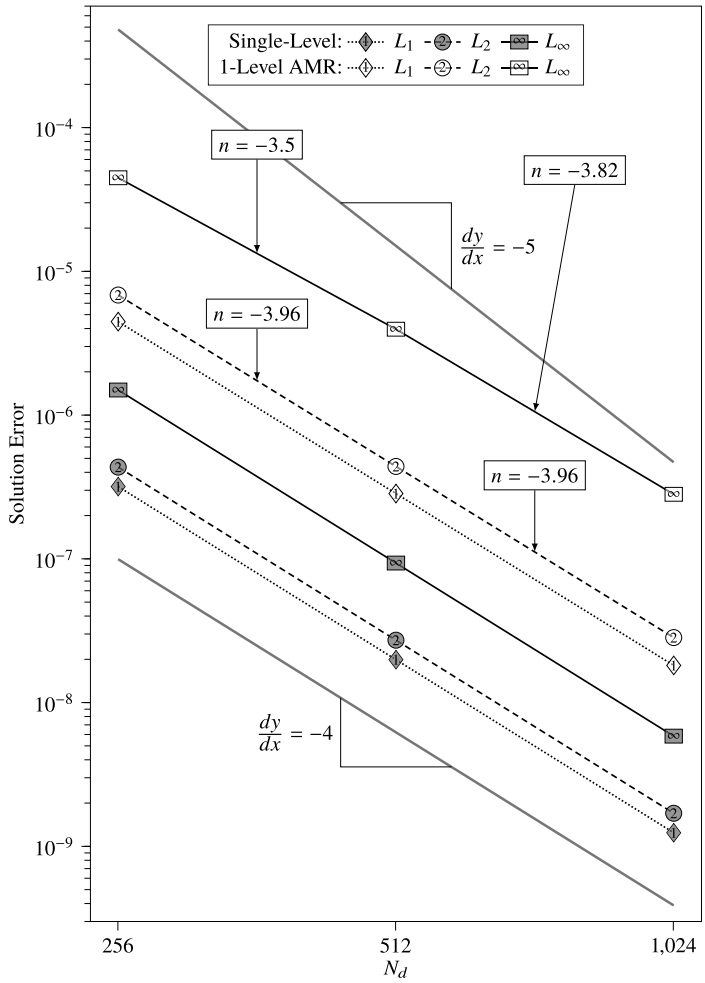

Fig. 12. Shear problem solution accuracy of x-momentum without face value limiting using both single-level grids and AMR grids. For the AMR grids, each AMR grid has one additional level of refinement. The resolution of the finest level of each AMR grid matches the resolution of the corresponding single-level grid.

to approximately 3.94, while the L_∞-norm continues to increase from 3.48 to 3.87 as the grid is refined. These figures demonstrate FVL does not impair convergence to fourth-order accuracy of the algorithm.

Verification of the DCL techniques is shown in Table 1. All solutions use FVL. The top of the table compares the convergence rates between solutions with and without DCL techniques for single-level solutions, i.e., no AMR. Similarly, the bottom of the table compares convergence rates for solutions that use an additional refinement level. This demonstrates that DC flattening and FCOR do not impair convergence to fourth-order accuracy for flow solutions on warped grids with or without AMR.

5.2. Conservation of species mass concentration

One important benefit to using FVMs is that they ensure conservation. However, the species mass concentration corrections described in Section 3.4 can violate the conservation of an individual species mass concentration, even when no mechanism for creating or destroying species, such as chemical reactions, are in place. Therefore, minimizing the impact of the species mass concentration corrections is of great importance. To test this, the shock tube problem described in Section 4.2.2 is used to evaluate the impact that the limiting techniques have on the conservation of species mass concentrations. The test does not use any reaction source terms, and the boundaries are walls in the x-direction and periodic in the y-direction to ensure mass, energy, and species are not added or removed at the boundaries.

To measure conservation, conserved variables are integrated over the domain at the start of the simulation and at solution time $t = 49$ μs for five different test cases. The values listed in Table 2 are the difference between the initial integrated value and the integrated value at the end of the solution as a percentage of the initial integrated value. The test cases use the different techniques as follows: Test 1 does not use FVL, DC flattening, or FCOR; Test 2 uses FVL only; Test 3 uses FVL

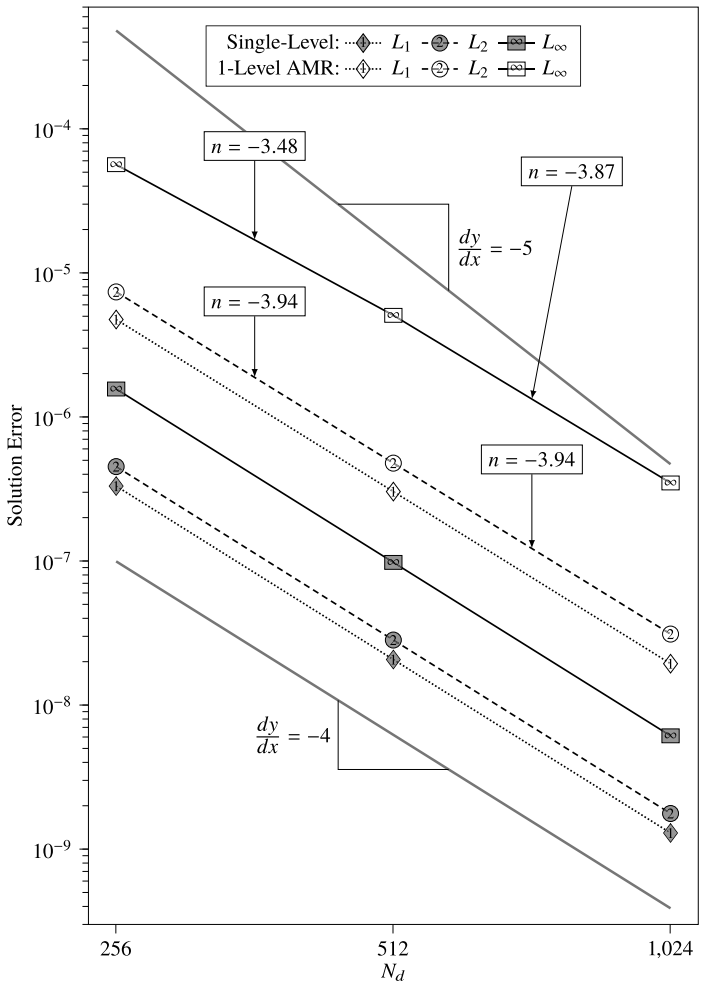

Fig. 13. Shear problem solution accuracy of x-momentum with face value limiting using both single-level grids and AMR grids. For the AMR grids, each AMR grid has one additional level of refinement. The resolution of the finest level of each AMR grid matches the resolution of the corresponding single-level grid.

and DC flattening; Test 4 uses FVL, DC flattening, and FCOR; and Test 5 is the solution from PeleC using the default fifth-order WENO-Z limiter. All Chord test cases use the PPM limiter, artificial viscosity, and interpolate/limit temperature and calculate density, as recommended in Section 4.2.2. Additionally, all Chord test cases utilize the species corrections detailed in Section 3.4.

The species mass concentrations for individual species are evidently not conserved in Tests 1 and 2. This loss of conservation is due to repeated corrections of the species mass concentrations with Eq. (33). The impact of the species corrections on conservation for Tests 3 and 4 appears to be negligible. In Test 5, conservation is violated for all variables. This could be due to a number of reasons. One possible explanation for the violation of conservation is insufficient limiting near the contact surface. The decoupling of species mass concentrations from the total mass from Eq. (49) could also explain the violation of conservation. The results show that the DCL techniques, as well as FVL, can significantly improve conservation of species mass concentrations.

5.3. The Shu-Osher problem

The Shu-Osher problem tests a shock-capturing scheme's ability to resolve small-scale flow features while capturing the shock. The Shu-Osher problem simulates the propagation of a normal shock wave into flow with density fluctuations. Unlike other test cases in this work, the fluid is assumed to be calorically-perfect and single species; this is done to avoid convergence issues associated with Eq. (30) and to use conditions that are consistent with other literature data [42]. The domain is periodic in the y-direction since the test problem is essentially 1-D. The domain is $L_x \times L_y = 10\ \text{m} \times 80/N_x\ \text{m}$, and the shock is initially located at $x_s = 1$ m. The domain length in the y-direction is varied to ensure $N_y = 8$ for all resolutions of N_x. The fluid relative to the initial shock location, x_s, is initialized as

Table 1
Convergence rates between consecutively refined grid resolutions for the shear flow problem without and with DCL techniques, labeled "w/o DCL" and "w/ DCL", respectively. The DCL techniques are the DC flattening and the FCOR. The convergence rates are based on the L_∞-, L_1-, and L_2-norms. All solutions use FVL.

AMR	Var	Grids	w/o DCL			w/ DCL		
			L_∞	L_1	L_2	L_∞	L_1	L_2
None	$J\rho u$	PC-C	4.00	4.00	4.00	4.00	4.00	4.00
		C-M	4.00	4.00	4.00	4.00	4.00	4.00
		M-F	4.00	4.00	4.00	4.00	4.00	4.00
	$J\rho v$	PC-C	4.00	4.00	4.00	4.00	4.00	4.00
		C-M	4.00	4.00	4.00	4.00	4.00	4.00
		M-F	4.00	4.00	4.00	4.00	4.00	4.00
	$J\rho e$	PC-C	4.00	4.00	4.00	4.00	4.00	4.00
		C-M	4.00	4.00	4.00	4.00	4.00	4.00
		M-F	4.00	4.00	4.00	4.00	4.00	4.00
1-Level	$J\rho u$	C-M	3.48	3.97	3.95	3.48	3.97	3.95
		M-F	3.87	3.97	3.94	3.87	3.97	3.94
	$J\rho v$	C-M	3.48	3.97	3.95	3.48	3.97	3.95
		M-F	3.87	3.97	3.94	3.87	3.97	3.94
	$J\rho e$	C-M	4.04	3.98	4.00	4.04	3.98	4.00
		M-F	3.83	3.97	3.97	3.83	3.97	3.97

Table 2
The percent change of the conservative solution variables integrated over the domain from the initial state to the state at solution time $t = 49$ μs for a shock tube problem.

Variable	Test 1	Test 2	Test 3	Test 4	Test 5
$J\rho$	3.365×10^{-12}	2.904×10^{-12}	3.411×10^{-12}	3.288×10^{-12}	1.964×10^{-6}
$J\rho e$	8.088×10^{-12}	9.082×10^{-12}	8.981×10^{-12}	9.217×10^{-12}	7.381×10^{-6}
Jc_{N_2}	1.318×10^{-1}	6.312×10^{-3}	3.379×10^{-13}	3.504×10^{-13}	7.752×10^{-7}
Jc_{O_2}	1.318×10^{-1}	6.312×10^{-3}	7.827×10^{-13}	8.239×10^{-13}	1.897×10^{-6}
Jc_{He}	8.796×10^{-2}	4.211×10^{-3}	2.088×10^{-12}	3.227×10^{-12}	3.261×10^{-6}

$$(\rho, u, p) = \begin{cases} (3.857143, 2.629369, 10.3333)\,, & \text{if } x \leq x_s\,, \\ (1 + 0.2\sin(5x), 0, 1)\,, & \text{otherwise}\,. \end{cases} \tag{66}$$

The solutions are run to a solution time of $t = 1.2$ s. Solutions are single-level (no AMR) with resolutions of $N_x = 256$, 512, 1024, and 2048. The "exact" solution is run with the PPM limiter on a very fine mesh of $N_x = 40960$. The CFL number is 0.75 in all simulations. All solutions are run with the base algorithm PPM limiter and artificial viscosity. Configurations are presented with the base algorithm limiting, FVL applied, and both FVL and DCL applied, shown as dashed lines, solid gray lines, and dotted lines, respectively.

The coarse solution ($N_x = 256$) is shown in Fig. 14. All three configurations in the figure show errors in the phase of the waves and amplitude relative to the "exact" solution. The figure shows that applying FVL causes more dissipation at the shock and that the amplitudes of the high-frequency waves are further under-predicted. The figure also shows very little difference between the FVL solution and the solution using both FVL and DCL. In the region further upstream, shown in Fig. 14c, the FVL solution does not capture the smooth extrema around $x \approx 2.3$ m. However, the extrema is captured when the DCL is added to the solution. At finer resolutions, there is virtually no difference between the "FVL" solutions and the "FVL & DCL" solutions. Only the "FVL" solutions will be shown for the remaining plots.

Fig. 15 shows the density profiles for the high-frequency waves behind the shock when the resolution is doubled. For the PPM profile, the wave amplitudes are much closer to the exact solution; however, there are slight errors in the phase of the waves. For the FVL profile, the errors in the phase of waves are corrected but more dissipation occurs at the shock wave, causing smaller amplitudes. A similar trend is seen at the $N_x = 1024$ resolution, shown in Fig. 16.

Density profiles at the finest resolution ($N_x = 2048$) are shown in Fig. 17. At this resolution, all of the solutions are virtually indistinguishable. The FVL method dissipates the shock more than the PPM limiter, but does not show significant differences in the high-frequency waves. Fig. 17b shows slight oscillations at the smooth extrema in the high-frequency waves for the PPM solution; these oscillations persist even when FVL is added.

Overall, these results show reasonable performance of the limiting techniques. The additional clipping at peaks caused by the limiting techniques is deemed a reasonable trade-off for monotonicity in temperature, which is critical for reacting flows. With AMR, smooth minima and maxima can still be accurately predicted where required.

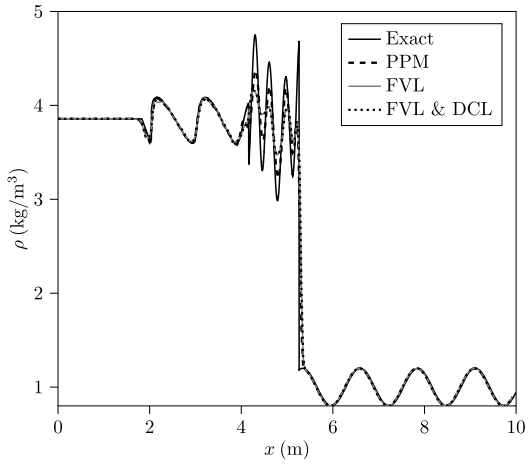

(a) Full domain.

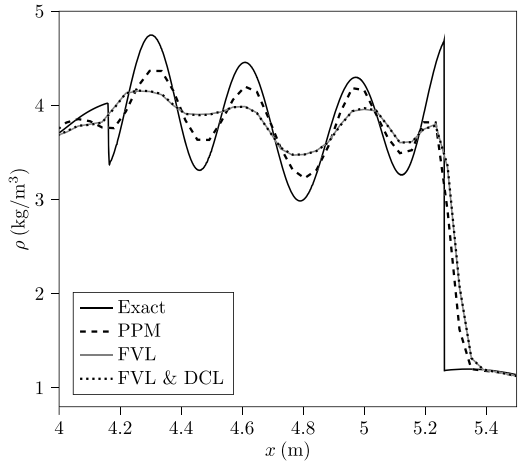

(b) High-frequency waves magnified.

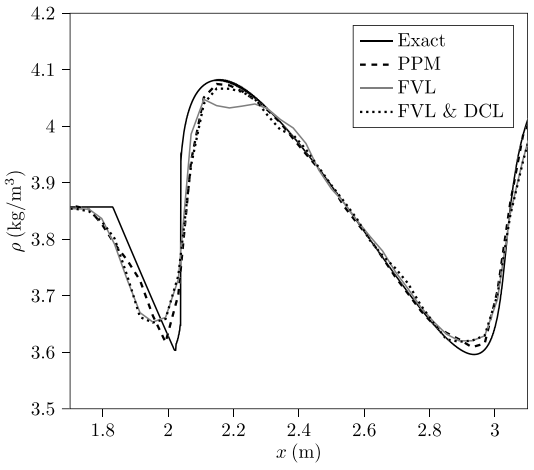

(c) Upstream smooth flow magnified.

Fig. 14. Shu-Osher density profiles for $N_x = 256$.

5.4. The double mach reflection problem

In the double Mach reflection problem, an incident shock at Mach 10 reflects off of a ramp, producing double Mach stems [35]. The Schwarz-Christoffel mapping, shown in Section 4.3.5, is used to model the ramp. This problem setup mirrors the

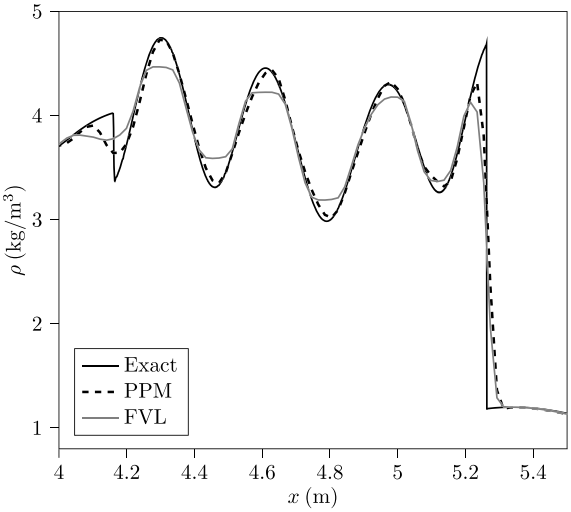

Fig. 15. Shu-Osher density profiles for $N_x = 512$.

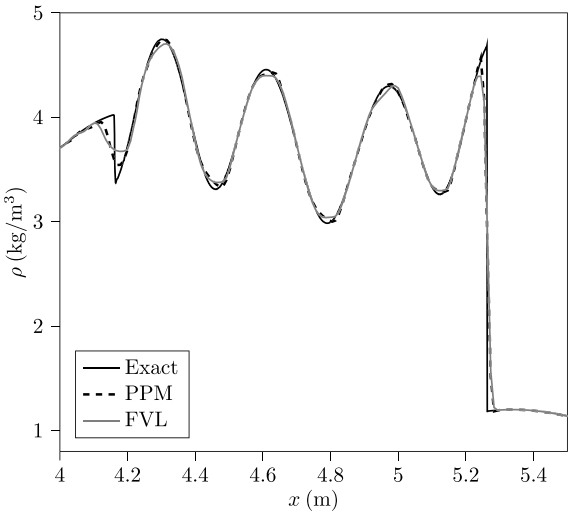

Fig. 16. Shu-Osher density profile for $N_x = 1024$.

problem setup by Guzik et al. [44]. The normalized pressure, density, and speed of sound in front of the shock are 1, 1.4, and 1, respectively. From Fig. 7, $\theta = 30°$, $l_r = 40$ cm, and $l_s = 8$ cm. The shock is initialized at 5 cm left of the start of the ramp, which is at $(0, 0)$. The base mesh size is 96×24. The fine grid solution has three additional refinement levels with refinement ratios of 4 for each level; the coarse grid solution only has two additional refinement levels. Refinement is based on gradients of density. The upper boundary condition is set to the freestream conditions before or after the shock. The location of the shock is estimated using the solution time. This boundary condition allows for a smaller domain in the wall normal direction but can introduce numerical artifacts into the solution.

Fig. 18 shows the double Mach reflection pseudo-color and contour plots of density at solution time $t = 0.025$. Figs. 18a and 18b are the fine grid solutions with and without the limiting techniques (FVL, DC flattening, and FCOR), respectively. Likewise, Figs. 18c and 18d are the corresponding solutions on the coarse grid. These plots show Kelvin-Helmholtz instabilities developing along the slip line. As expected, these instabilities are more dissipated in the coarse grid solutions. Aside from differences along the slip line, attributed to the chaotic nature of the instabilities, the differences from using the additional limiting techniques are negligible. This demonstrates that the limiting techniques do not significantly impact the modeling of small-scale structures in discontinuous flows.

5.5. Oblique detonation waves

We report the results for three test cases of ODWs are obtained by applying the all limiting techniques (FVL, DC flattening, and FCOR) to the base algorithm, Chord. The present solutions are compared with literature data. For all cases studied

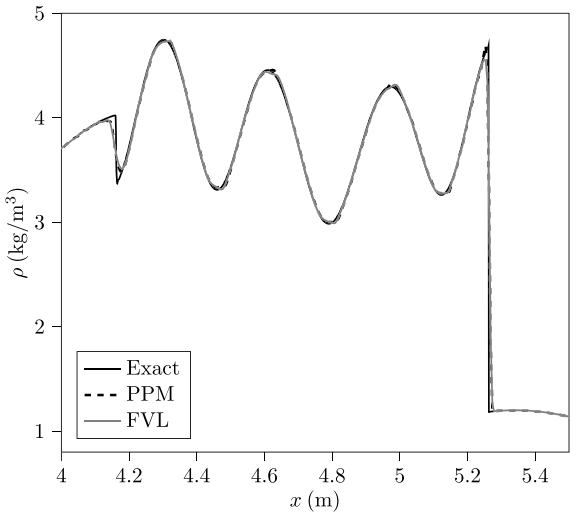

(a) High-frequency waves magnified.

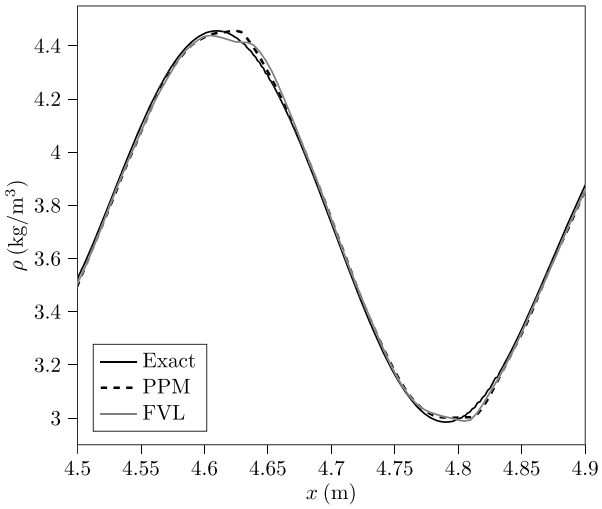

(b) High-frequency waves further magnified.

Fig. 17. Shu-Osher density profiles for $N_x = 2048$.

herein, the computational domain is shown in Figs. 7 and 19, with the wedge angle denoted by θ and the freestream Mach number denoted by Ma_∞. In all tests, a stoichiometric mixture of hydrogen and air ($H_2 : O_2 : N_2/2 : 1 : 3.76$) flows from left to right at high Mach number and encounters a ramp. Heating from the resultant oblique shock induces deflagration after an induction delay. Because the combustion is constrained by the wall of the ramp, compression waves are produced that propagate inwards while coalescing to ultimately produce a detonation wave. The transition in steady 2-D space is analogous to deflagration-to-detonation (DDT) observed in unsteady 1-D space when deflagration is initiated at a wall, except that thermal diffusion is not required for flame propagation in an ODW. The observed structures match those described by Li et al. [49].

As shown in Section 4.3.5, a Schwarz-Christoffel mapping transformation is used to model the wedge. The wedge tip is at $(0, 0)$ in physical space. By contrast, studies from the literature commonly use a Cartesian grid with an angled velocity vector, as shown in Fig. 19. In all simulations, the top boundary is sufficiently far from the wall as to not interact with waves produced in the simulations. Supersonic inflow and outflow boundary conditions are used along with slip boundaries at the walls. Solutions obtained with Chord use AMR to reduce errors where required, especially near discontinuities, while minimizing computational cost elsewhere. Refinement is based on gradients of temperature; additionally, refinement is fixed in the layer of cells adjacent to the wall.

Comparisons are made with three different ODW cases from the literature. The wedge angle, freestream conditions, domain lengths, number of reactions in the reference reaction mechanism, number of reactions in the Chord reaction mechanism, and literature reference are provided in Table 3. The footnotes list the species considered in the reaction mechanism.

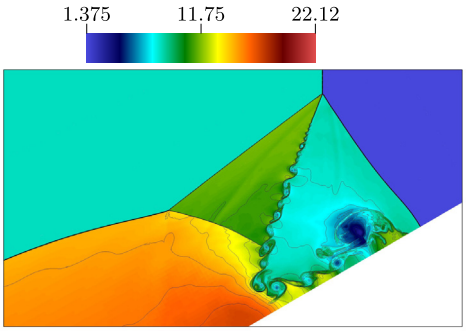

(a) Fine grid solution with FVL and DCL.

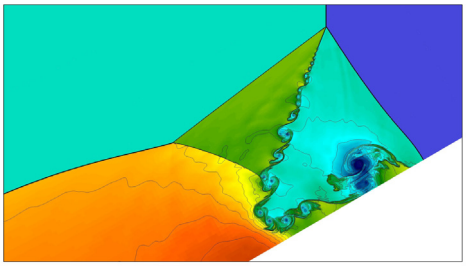

(b) Fine grid solution without FVL and DCL.

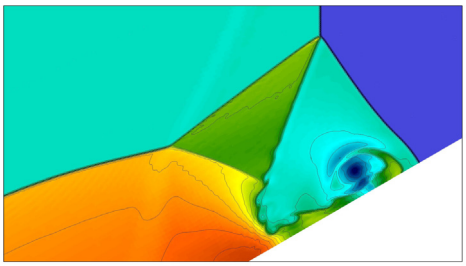

(c) Coarse grid solution with FVL and DCL.

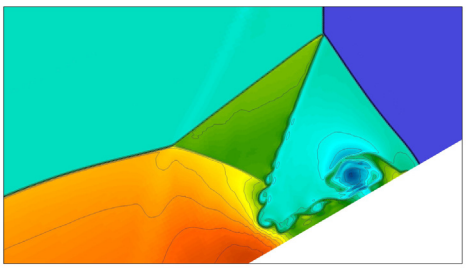

(d) Coarse grid solution without FVL and DCL.

Fig. 18. Pseudo-color and contour plots of density and corresponding legend for the double Mach reflection at solution time $t = 0.025$. Viewing window is from (11 cm, 10 cm) to (24 cm, 18 cm) in physical space.

In all cases, the fluid is a stoichiometric mixture of hydrogen and air, and diffusion is neglected. The same reaction mechanisms used in the references are also used in Chord except for Case 1, where the 12-step model from Thaker and Chelliah [50] is used. When necessary, the Chord results in this section are taken from a rotated physical domain to make comparisons with literature possible. See the axis in Fig. 19 for reference.

5.5.1. Case 1: $\mathrm{Ma}_\infty = 8, \theta = 29°$

The first case is taken from the work by Li et al. [49] with $\mathrm{Ma}_\infty = 8$, $\theta = 29°$. The reference study uses a uniform grid spacing of $\Delta x = \Delta y = 6$ μm and a two-step reaction mechanism. The solution by Chord is obtained with

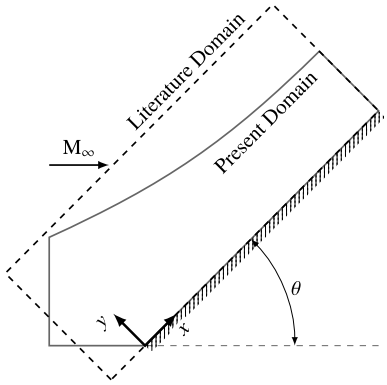

Fig. 19. Comparison between wedge domains.

Table 3
List of each reference ODW case and relevant details.

Case	θ	Ma_∞	p_∞ (atm)	T_∞ (K)	l_r (mm)	l_s (mm)	N_r-Ref	N_r-Chord	Ref.
1	29°	8	1	300	4	0.5	2[a]	12[b]	[49]
2	27°	9.3	1	300	5	1	12[b]	12[b]	[50]
3	15°	4.3	0.5527	1021	60	5	23[c]	23[c]	[51]

[a] Two-step reaction mechanism involving 5 species: H_2, O_2, N_2, H_2O, and a representation for intermediate species [49].
[b] 12-step reaction mechanism involving 8 species: H_2, O_2, N_2, H_2O, HO_2, OH, O, and H [50].
[c] 23-step reaction mechanism involving 11 species: H_2, O_2, N_2, H_2O, HO_2, OH, H_2O_2, O, H, N, and NO [52].

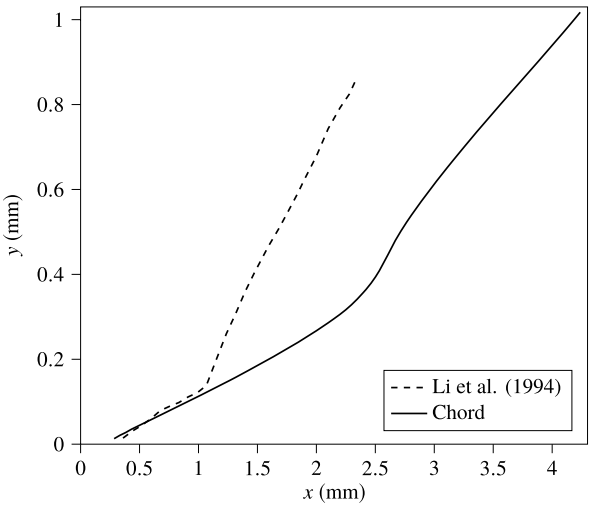

Fig. 20. Oblique shock location comparison for Case 1.

one additional refinement level with a refinement ratio of 4. The base mesh size is 192×96 (finest level grid spacing: $(\Delta x, \Delta y) \approx (5.86\ \mu m, 5.86\ \mu m)$). The 12-step mechanism described by Thaker and Chelliah [50] models the reaction.

Comparisons of the OSW and ODW profiles are shown in Fig. 20. There is poor agreement in the length of the induction region and the slopes of the detonation waves. The disparate rates of heat release behind the detonation, caused by the different reaction models, account for the observed differences; the reaction model used by Li et al. in their early work is limited in capability. The reference predicts increased heat addition, which causes a more abrupt transition and steeper detonation wave due to a shorter induction region. Regardless, the geometry of the detonation is otherwise similar to the reference. In particular, the same steepening of the detonation, just after transition, can be observed in the reference and leads to a small region of subsonic flow.

5.5.2. Case 2: $Ma_\infty = 9.3$, $\theta = 27°$

The second case reproduces a problem studied by Thaker and Chelliah [50]. The parameters of the setup from the reference are $\theta = 27°$, $Ma_\infty = 9.3$, and a grid spacing of $(\Delta x, \Delta y) = (25\ \mu m, 16.6\ \mu m)$. In Chord, the base mesh is 192×48

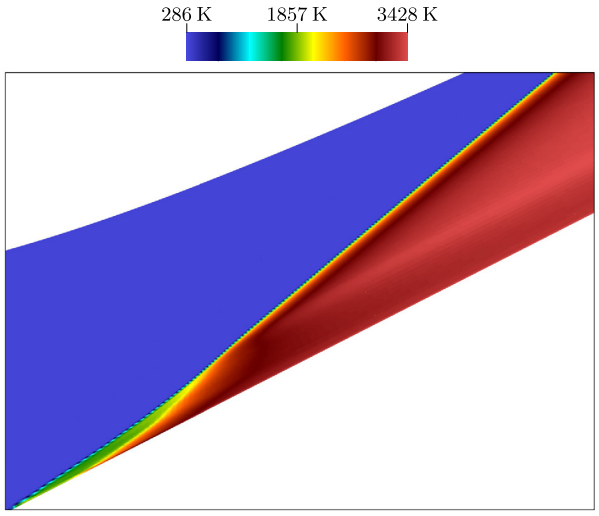

Fig. 21. Pseudo-color of temperature and corresponding legend for Case 2. Viewing window is from $(-4 \times 10^{-2}$ mm, 0 mm) to (4 mm, 3 mm) in physical space.

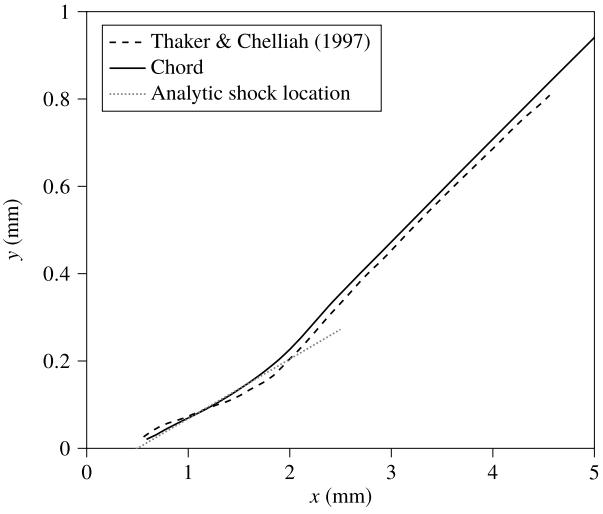

Fig. 22. Oblique shock location comparison for Case 2.

with one additional refinement level with refinement ratio of 4 (finest level grid spacing: $(\Delta x, \Delta y) \approx (7.8\ \mu\text{m}, 7.8\ \mu\text{m})$). Additionally, a solution with a comparable resolution to the reference uses a refinement ratio of 2 instead of 4 (finest level grid spacing: $(\Delta x, \Delta y) \approx (15.6\ \mu\text{m}, 15.6\ \mu\text{m})$); this is denoted as the "coarse" solution. In both the reference and the Chord simulations, the 8 species, 12-step reaction mechanism described by Thaker and Chelliah [50] is used to model the chemical reactions. For boundary conditions, the reference enforces $\partial T/\partial y = 0$ and $\partial p/\partial y = 0$ whereas no such restrictions are used in Chord. Fig. 21 shows the steady-state temperature pseudo-color plot of the finer solution. The green area near the corner of the wedge is the induction zone behind the OSW; the following red region represents the heat release and fully coupled ODW.

The OSW and ODW profiles are compared in Fig. 22. Interestingly, the oblique shocks have different slopes while the slopes of the detonations are in good agreement. In all other comparisons, Chord matches the oblique shock angle from the literature. Furthermore, oblique shock predictions should reasonably match analytical theory for a calorically-perfect gas with frozen composition. This curve is also plotted as a dotted line which is in much better agreement with Chord. The reference predicts an abrupt transition whereas Chord predicts a much more gradual one.

Temperature profiles across the wedge, shown in Fig. 23, provide more information. Across an ODW, one expects that the temperature profile would consist of the following: a nonreactive shock, signaled by an initial discontinuous temperature rise; an induction zone, signaled by a temperature plateau; and finally, a region of heat release indicated by monotonic temperature rise, either in the form of a deflagration wave for regions near the wall or a more energetic release following a detonation. Accordingly, the temperature profile predicted by Chord in Fig. 23 consists of an oblique shock, induction

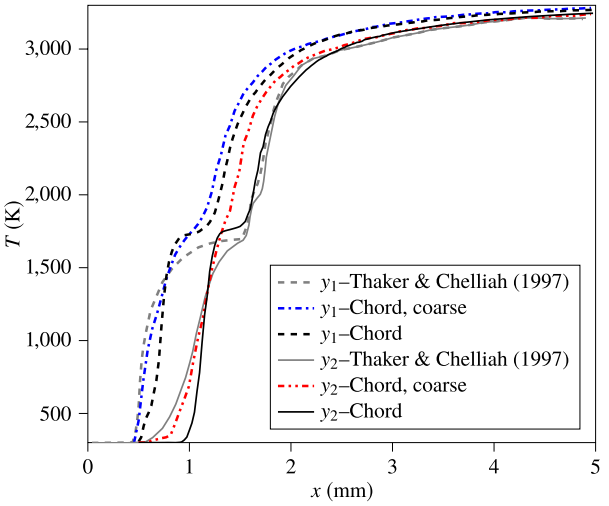

Fig. 23. Temperature profiles along varying wall normal planes for Case 2; $y_1 = 33.2$ μm and $y_2 = 83$ μm.

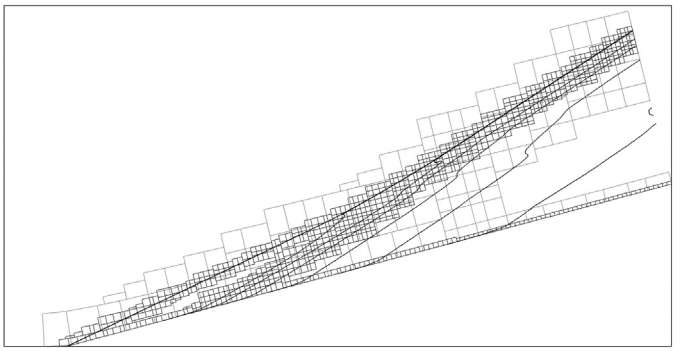

Fig. 24. Mesh patches overlying temperature contour lines. The lighter boxes are the first refined level and the darker boxes are the second refined level. The darker lines are contours of temperature. The mesh refines around temperature increases associated with the oblique shock and regions of significant heat release in the flow.

zone, and heat release. The coarse solution temperature profiles from Chord show that the resolution used in the reference is insufficient to capture the induction zone behind the nonreactive shock. The temperature profiles from the reference solution smear the oblique shock and heat release with no distinct induction region. The reference solution also shows the heat release occurs at the same streamwise location for different wall normal planes, which is inconsistent with the expected physics. In summary, there is some doubt about the numerically accuracy of the reference solution in the vicinity of the oblique shock and induction zone.

5.5.3. Case 3: $\mathrm{Ma}_\infty = 4.3$, $\theta = 15°$

The third ODW reference was simulated by Wang et al. [51]. In this problem, $\theta = 15°$ and $\mathrm{Ma}_\infty = 4.3$. The reference also utilizes AMR with a grid spacing of $(\Delta x, \Delta y) = (25\ \mu\mathrm{m}, 25\ \mu\mathrm{m})$ on the finest grid level. A base mesh size of 200×80 is used in Chord with two additional refinement levels, each with a refinement ratio of 4 (finest level grid spacing: $(\Delta x, \Delta y) \approx (20.3\ \mu\mathrm{m}, 20.3\ \mu\mathrm{m})$). When the shock structures are developed, the AMR grid appears as shown in Fig. 24.

In both the reference and the Chord simulation, the 11 species, 23-step reaction mechanism from CHEMKIN [52] is employed to model the chemical reactions.

The nonreactive shock and flame profiles are compared in Fig. 25. The flame location is identified based on a critical temperature of $T = 2070$ K; this temperature corresponds to the temperature at the end of the Zel'dovich-von Neumann-Döring (ZND) induction zone. The shock profiles from the present study are in very good agreement with slight deviations near the outlet. The flame locations differ slightly in the near wall region. The reference predicts a flame that appears almost perpendicular to the wall whereas Chord predicts a steep angle leading into the wall.

Since the walls are slip walls, the most reasonable expectation for the flame shape near the wall is a straight line with a slope similar to the ODW. Positive curvature is expected as one moves away from the wall due to compression waves that result from constrained deflagration. The solutions from both codes deviate from an expected profile. The reference does not detail how temperature is handled at the wall, but enforcement of $\partial T/\partial y = 0$ at the wall is consistent with the shape of

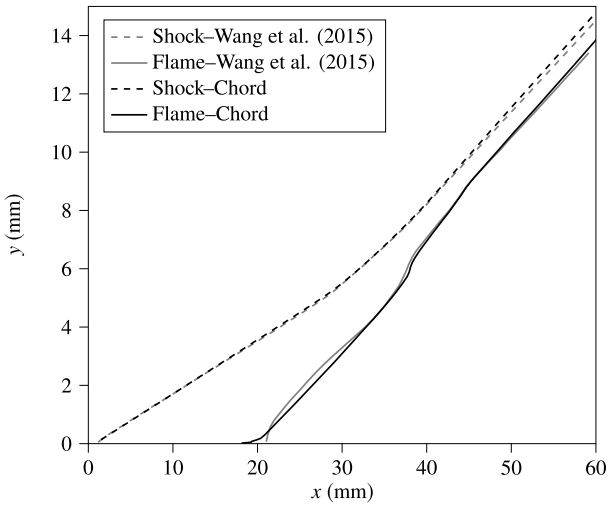

Fig. 25. Shock and flame location comparison for Case 3.

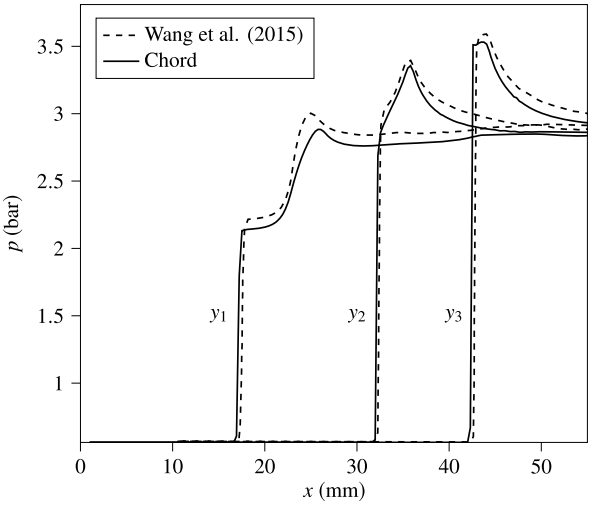

Fig. 26. Pressure profiles along varying wall normal planes for Case 3; $y_1 = 3$ mm, $y_2 = 6$ mm, and $y_3 = 9$ mm.

the flame profile near the wall in Fig. 25. In Chord, cells adjacent to the wall suffer from overheating at the oblique shock, shortening the induction zone length adjacent to the wall. When solving the jump conditions across a shock, the interior scheme relies on an error cancellation property in the fluxes on each side of a cell. However, the exact momentum flux at the wall is used as a boundary condition so the errors do not cancel. The error manifests as the observed heating; this effect is described in detail by Woodward [47]. Overheating at the wall is purely numerical and not representative of any physical phenomena; it scales with mesh resolution and does not affect convergence. The overheating at the wall would vanish if the viscous scales were resolved near the wall.

Pressure and temperature profiles at varying wall normal planes are shown in Figs. 26 and 27, respectively. From the pressure profiles, it is evident that the y_1 curve shows deflagration, y_2 is near transition, and at y_3 a single pressure rise of a detonation is observed. The induction zone is the plateau in the temperature profile following the shock. This induction zone becomes smaller as the distance from the wall grows and is quite brief in the detonation (y_3). The peaks in pressure correspond to the heat release from the reactions. For the y_1 profile, the separation between the initial pressure rise and the pressure peak means the nonreactive shock is followed by a set of deflagration waves. The y_3 profile captures the oblique detonation since the oblique shock and the heat release are fully coupled. The profile at y_2 corresponds to an intermediate structure between the decoupled and fully coupled nonreactive and reactive shocks. The Chord solution agrees well with the reference solution, and the profiles are consistent with the observations of Li et al. [49], except the detonation induction zone is clearly seen by both predictions for the present case (y_3 in Fig. 27).

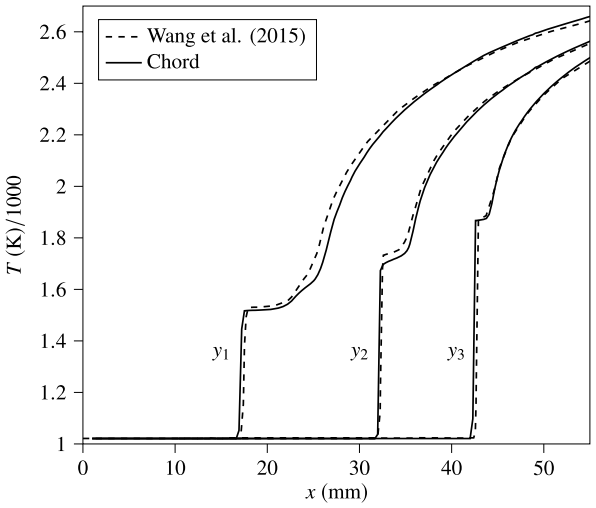

Fig. 27. Temperature profiles along varying wall normal planes for Case 3; $y_1 = 3$ mm, $y_2 = 6$ mm, and $y_3 = 9$ mm.

6. Conclusions and future work

In this study, we devised, developed, and tested new limiting techniques for reducing numerical oscillations in a fourth-order FVM algorithm for solving thermally-perfect, multispecies, compressible fluid flows. The capability of these techniques is verified with problems containing strong shock and detonation waves. Furthermore, a shock tube solution indicates that limiting temperature and pressure, applying FVL, and using DC flattening and FCOR provides the least oscillatory solution while maintaining conservation of species mass concentrations in cold mixing flows. We verify that the techniques do not engage in regions of smooth flow and do not negatively impact the accuracy of the underlying numerical algorithm. The algorithm is applied to solve the Shu-Osher and double Mach reflection problems and a series of ODWs; these results demonstrate that the techniques successfully remove spurious oscillations while meeting the design criteria. Future work will focus on modeling these problems in three dimensions and investigating the physics and structure of the cellular detonations in normal and oblique detonation problems.

Declaration of competing interest

The authors declare that they have no known competing financial interests or personal relationships that could have appeared to influence the work reported in this paper.

Acknowledgements

This research was supported by Department of Defense United States Air Force (DOD-USAF-Air Force) under the award number FA9550-18-1-0057 and by National Science Foundation under the award number 1723191.

References

[1] Z.J. Wang, K. Fidkowski, R. Abgrall, F. Bassi, D. Caraeni, A. Cary, H. Deconinck, R. Hartmann, K. Hillewaert, H.T. Huynh, N. Kroll, G. May, P.-O. Persson, B. van Leer, M. Visbal, High-order CFD methods: current status and perspective, Int. J. Numer. Methods Fluids 72 (8) (2013) 811–845.
[2] Z.J. Wang, High-order computational fluid dynamics tools for aircraft design, Philos. Trans. R. Soc. A, Math. Phys. Eng. Sci. 372 (2022) (2014).
[3] 5th international workshop on high order CFD methods, https://how5.cenaero.be/, Jan 2018.
[4] P. Colella, M. Sekora, A limiter for PPM that preserves accuracy at smooth extrema, J. Comput. Phys. 227 (15) (2008) 7069–7076.
[5] P. McCorquodale, P. Colella, A high-order finite-volume method for conservation laws on locally refined grids, Commun. Appl. Math. Comput. Sci. 6 (1) (2011) 1–25.
[6] A.K. Henrick, T.D. Aslam, J.M. Powers, Mapped weighted essentially non-oscillatory schemes: achieving optimal order near critical points, J. Comput. Phys. 207 (2) (2005) 542–567.
[7] A.K. Henrick, T.D. Aslam, J.M. Powers, Simulations of pulsating one-dimensional detonations with true fifth order accuracy, J. Comput. Phys. 213 (1) (2006) 311–329.
[8] S.-H. Yoon, C. Kim, K.-H. Kim, Multi-dimensional limiting process for three-dimensional flow physics analyses, J. Comput. Phys. 227 (12) (2008) 6001–6043.
[9] J.S. Park, C. Kim, Multi-dimensional limiting process for finite volume methods on unstructured grids, Comput. Fluids 65 (2012) 8–24.
[10] R.W. Houim, K.K. Kuo, A low-dissipation and time-accurate method for compressible multi-component flow with variable specific heat ratios, J. Comput. Phys. 230 (23) (2011) 8527–8553.
[11] S. Karni, Hybrid multifluid algorithms, SIAM J. Sci. Comput. 17 (5) (1996) 1019–1039.
[12] R. Abgrall, S. Karni, Computations of compressible multifluids, J. Comput. Phys. 169 (2) (2001) 594–623.

[13] P.C. Ma, Y. Lv, M. Ihme, An entropy-stable hybrid scheme for simulations of transcritical real-fluid flows, J. Comput. Phys. 340 (2017) 330–357.
[14] G. Billet, R. Abgrall, An adaptive shock-capturing algorithm for solving unsteady reactive flows, Comput. Fluids 32 (10) (2003) 1473–1495.
[15] K.H. Kim, C. Kim, Accurate, efficient and monotonic numerical methods for multi-dimensional compressible flows: Part II: Multi-dimensional limiting process, J. Comput. Phys. 208 (2) (2005) 570–615.
[16] E.M. Taylor, M. Wu, M.P. Martin, Optimization of nonlinear error for weighted essentially non-oscillatory methods in direct numerical simulations of compressible turbulence, J. Comput. Phys. 223 (1) (2007) 384–397.
[17] B. Thornber, A. Mosedale, D. Drikakis, D. Youngs, R.J.R. Williams, An improved reconstruction method for compressible flows with low mach number features, J. Comput. Phys. 227 (10) (2008) 4873–4894.
[18] H.-M. Kang, K.H. Kim, D.-H. Lee, A new approach of a limiting process for multi-dimensional flows, J. Comput. Phys. 229 (19) (2010) 7102–7128.
[19] T. Schmitt, L. Selle, A. Ruiz, B. Cuenot, Large-eddy simulation of supercritical-pressure round jets, AIAA J. 48 (9) (2010) 2133–2144.
[20] H. Terashima, M. Koshi, Approach for simulating gas–liquid-like flows under supercritical pressures using a high-order central differencing scheme, J. Comput. Phys. 231 (20) (2012) 6907–6923.
[21] S.M. Guzik, X. Gao, L.D. Owen, P. McCorquodale, P. Colella, A freestream-preserving fourth-order finite-volume method in mapped coordinates with adaptive-mesh refinement, Comput. Fluids 123 (2015) 202–217.
[22] S.M. Guzik, X. Gao, C. Olschanowsky, A high-performance finite-volume algorithm for solving partial differential equations governing compressible viscous flows on structured grids, Comput. Math. Appl. 72 (2016) 2098–2118.
[23] X. Gao, L.D. Owen, S.M.J. Guzik, A parallel adaptive numerical method with generalized curvilinear coordinate transformation for compressible Navier-Stokes equations, Int. J. Numer. Methods Fluids 82 (2016) 664–688.
[24] L.D. Owen, S.M. Guzik, X. Gao, A high-order adaptive algorithm for multispecies gaseous flows on mapped domains, Comput. Fluids 170 (2018) 249–260.
[25] C.-W. Shu, S. Osher, Efficient implementation of essentially non-oscillatory shock-capturing schemes, II, in: Upwind and High-Resolution Schemes, Springer, 1989, pp. 328–374.
[26] S. Gordon, B.J. McBride, Computer Program for Calculation of Complex Chemical Equilibrium Compositions and Applications I. Analysis, Reference Publication, vol. 1311, NASA, 1994.
[27] B.J. McBride, S. Gordon, Computer Program for Calculation of Complex Chemical Equilibrium Compositions and Applications II. Users Manual and Program Description, Reference Publication, vol. 1311, NASA, 1996.
[28] M. Adams, P. Colella, D.T. Graves, J.N. Johnson, H.S. Johansen, N.D. Keen, T.J. Ligocki, D.F. Martin, P.W. McCorquodale, D. Modiano, P.O. Schwartz, T.D. Sternberg, B. Van Straalen, Chombo Software Package for AMR Applications - Design Document, Tech. Rep. LBNL-6616E, Lawrence Berkeley National Laboratory, 2014.
[29] H. Lomax, T.H. Pulliam, D.W. Zingg, Fundamentals of Computational Fluid Dynamics, 1st edition, Scientific Computation, Springer-Verlag Berlin Heidelberg, 2001.
[30] C. Hirsch, Numerical Computation of Internal and External Flows: The Fundamentals of Computational Fluid Dynamics, Elsevier, 2007.
[31] B. Riviere, Discontinuous Galerkin Methods for Solving Elliptic and Parabolic Equations: Theory and Implementation, SIAM, 2008.
[32] T.H. Pulliam, D.W. Zingg, Fundamental Algorithms in Computational Fluid Dynamics, 1st edition, Scientific Computation, Springer International Publishing, New Delhi, India, 2014.
[33] J.D. Lambert, Numerical Methods for Ordinary Differential Systems, John Wiley & Sons, New York, 1991.
[34] C. Chaplin, P. Colella, A single-stage flux-corrected transport algorithm for high-order finite-volume methods, Commun. Appl. Math. Comput. Sci. 12 (1) (2017) 1–24.
[35] P.R. Woodward, P. Colella, The numerical simulation of two-dimensional fluid flow with strong shocks, J. Comput. Phys. 54 (1) (1984) 115–173.
[36] P. Colella, Multidimensional upwind methods for hyperbolic conservation laws, J. Comput. Phys. 87 (1) (1990) 171–200.
[37] R.P. Brent, An algorithm with guaranteed convergence for finding a zero of a function, Comput. J. 14 (4) (1971) 422–425.
[38] L.D. Owen, S.M. Guzik, X. Gao, A fourth-order finite-volume algorithm for compressible flow with chemical reactions on mapped grids, in: 23rd AIAA Computational Fluid Dynamics Conference, AIAA 2017-4498, AIAA AVIATION Forum, 2017.
[39] P. Colella, P.R. Woodward, The piecewise parabolic method (PPM) for gas-dynamical simulations, J. Comput. Phys. 54 (1) (1984) 174–201.
[40] M.J. Berger, P. Colella, Local adaptive mesh refinement for shock hydrodynamics, J. Comput. Phys. 82 (1) (1989) 64–84.
[41] PeleC, version 00 (2017), https://www.osti.gov//servlets/purl/1374142.
[42] E. Motheau, J. Wakefield, Investigation of finite-volume methods to capture shocks and turbulence spectra in compressible flows, Commun. Appl. Math. Comput. Sci. (2020), forthcoming, preprint version at https://arxiv.org/abs/1902.06665.
[43] A.A.I. Peer, A. Gopaul, M.Z. Dauhoo, M. Bhuruth, A new fourth-order non-oscillatory central scheme for hyperbolic conservation laws, Appl. Numer. Math. 58 (5) (2008) 674–688.
[44] S.M. Guzik, P. McCorquodale, P. Colella, A freestream-preserving high-order finite-volume method for mapped grids with adaptive-mesh refinement, in: 50th AIAA Aerospace Sciences Meeting, AIAA 2012-0574, AIAA, 2012.
[45] L.F. Figueria da Silva, B. Deshaies, Stabilization of an oblique detonation wave by a wedge: a parametric numerical study, Combust. Flame 121 (1) (2000) 152–166.
[46] G. Billet, Improvement of convective concentration fluxes in a one step reactive flow solver, J. Comput. Phys. 204 (1) (2005) 319–352.
[47] P.R. Woodward, Piecewise-Parabolic Methods for Astrophysical Fluid Dynamics, Springer, Netherlands, Dordrecht, 1986, pp. 245–326.
[48] P. Colella, M.R. Dorr, J.A.F. Hittinger, D.F. Martin, High-order finite-volume methods in mapped coordinates, J. Comput. Phys. 230 (2011) 2952–2976.
[49] C. Li, K. Kailasanath, E.S. Oran, Detonation structures behind oblique shocks, Phys. Fluids 6 (4) (1994) 1600–1611.
[50] A.A. Thaker, H.K. Chelliah, Numerical prediction of oblique detonation wave structures using detailed and reduced reaction mechanisms, Combust. Theory Model. 1 (4) (1997) 347–376.
[51] T. Wang, Y. Zhang, H. Teng, Z. Jiang, H.D. Ng, Numerical study of oblique detonation wave initiation in a stoichiometric hydrogen-air mixture, Phys. Fluids 27 (9) (2015) 096101.
[52] R.J. Kee, R.M. Ruply, E. Meeks, J.A. Miller, Chemkin-III: a FORTRAN chemical kinetics package for the analysis of gas-phase chemical and plasma kinetics, Technical Report SAND96-8216, Sandia National Laboratories, Livermore, 1996.